

---

# SynVA: A Modular Toolkit for Vessel Generation and Aneurysm Editing

---

Marten J. Finck\*<sup>1</sup>    Niklas C. Koser\*<sup>1</sup>    Sarker M. Mahfuz<sup>1</sup>    Tameem Jahangir<sup>2</sup>  
Jon E. Wilhelm<sup>1</sup>    Daniel Behme<sup>3</sup>    Naomi Larsen<sup>4</sup>    Wojtek Palubicki<sup>5</sup>  
Sylvia Saalfeld<sup>2</sup>    Sören Pirk<sup>1</sup>

<sup>1</sup> Visual Computing and Artificial Intelligence, Kiel University, Germany

<sup>2</sup> Institute for Medical Informatics and Statistics, Kiel University, Germany

<sup>3</sup> Clinic for Neuroradiology, Medical Faculty, Magdeburg University, Germany

<sup>4</sup> Department of Radiology and Neuroradiology, University Hospital Schleswig-Holstein, Germany

<sup>5</sup> Faculty of Mathematics and Computer Science, Adam Mickiewicz University, Poland

## Abstract

Intracranial aneurysms (IAs), characterized by unpredictable growth and risk of rupture, are a major cause of stroke and can lead to life-threatening hemorrhages with high mortality and long-term disability. With aging populations, the incidence and overall burden of cerebrovascular diseases are expected to increase, highlighting the need for scalable approaches to analyze complex medical data and improve population-level understanding of these conditions. While digital twins and deep learning offer promising avenues for improving diagnosis, prognosis, and treatment, their effectiveness is limited by the scarcity of large-scale, high-quality medical data and corresponding labels. We present **Synthetic VAsculature (SynVA)**, a modular toolkit for vascular mesh generation and anatomically consistent aneurysm synthesis. SynVA combines novel flow-matching-based methods for generating healthy vessel meshes with learning-based approaches for anatomy-conditioned aneurysm mesh generation — aneurysms are computed from pre-existing vascular geometries rather than being generated in isolation. In addition, we introduce the SynVA procedural model for vascular and aneurysm synthesis based solely on physiological principles and statistical priors, which enables the generation of large-scale datasets (e.g., for the training of mesh-based generative models). To this end, we release a dataset of 50,000 fully labeled mesh samples for a variety of downstream vision tasks, such as semantic segmentation. Extensive quantitative and qualitative evaluations demonstrate that SynVA generates realistic vessel geometries and anatomically plausible aneurysms. Specifically, our experiments indicate that some methods produce aneurysm shapes more aligned with expert human perception while others perform better on quantitative similarity metrics with reconstructions of real aneurysms.

## 1 Introduction

Intracranial aneurysms (IAs) are acquired pathological dilatations of cerebral arteries that arise from structural alterations of the vessel wall and a resulting imbalance between tensile wall strength and local hemodynamic stress [22, 23, 66, 72]. Typically, IAs are asymptomatic and therefore often remain undetected. Only a small fraction (approximately 10-15 %) shows neurological symptoms, usually

---

\*Contributed equally to this work.

caused by compression of cranial nerves or adjacent cerebral structures [22, 37, 72]. Despite their frequently silent nature, IAs are clinically relevant due to their unpredictable growth and persistent risk of rupture [37, 66]. The resulting hemorrhage, most commonly subarachnoid hemorrhage (SAH), leads to sudden severe headache, nausea, vomiting, loss of consciousness, and other neurological deficits, and is associated with high morbidity and mortality [22, 23, 37, 66, 72]. In numbers: The overall prevalence of IAs is estimated at approximately 5.4% [63], with roughly 1 in 50 individuals in the United States having an unruptured aneurysm. The annual rupture incidence is reported at 8-10 cases per 100,000 individuals, corresponding to approximately 30,000 ruptures per year in the United States alone [6]. Rupture outcomes are frequently severe: mortality rates range between 25 and 50%, with approximately 15% of patients dying before reaching hospital care. Among survivors, 50-66% suffer from long-term neurological deficits, while only about 30% achieve a favorable outcome [6, 23, 37]. These figures underscore the critical importance of accurate early risk assessment, timely diagnosis, and targeted therapeutic intervention. From a healthcare perspective, preventive strategies are also economically favorable, as treatment after rupture is substantially more costly than early intervention [6]. Risk factors for IA formation and rupture include both aneurysm-specific and patient-specific characteristics. These comprise morphological parameters (e.g., size, aspect ratio, irregularity), anatomical location, hypertension, age, sex (with higher prevalence in females), geographic and ethnic factors, prior SAH, family history, and smoking status [14, 23, 52, 66, 72].

In this context, digital twins (DTs), i.e., virtual counterparts of real anatomical structures that combine statistical, data-driven, and mechanistic models to reflect physiological behavior and dynamics, offer a promising route toward more precise patient-specific prognosis and treatment planning [17, 83, 89]. Since both hemodynamics and aneurysm geometry, individually and in combination, are highly relevant for the dynamic behavior of IAs, there is growing interest in in-silico studies using 3D DTs of vascular systems with IAs, for instance to estimate wall shear stress (WSS) via computational fluid dynamics (CFD) [14, 66, 72]. In parallel, deep learning approaches for accelerated flow prediction or IA segmentation are gaining importance [45, 74, 77], further underscoring the need for large, labeled 3D datasets of IAs and their parent vessels. However, real-world datasets remain limited in size [11, 34, 46, 82, 94, 102], and reconstruction from medical imaging data is challenging, requires expert knowledge, and is prone to errors [2, 43, 53]. As a result, synthetic 3D data generation is increasingly viewed as a viable strategy to provide labeled data for downstream applications while improving not only quantity but also diversity [90, 98]. Yet, model-driven procedural approaches remain scarce, and existing methods often still rely on real data [12, 38, 56, 68]. More recent data-driven AI methods for vascular synthesis tend to focus either on aneurysm generation [15] or on vessel generation [20], but not on a unified end-to-end framework. Motivated by these challenges, we introduce **Synthetic VAsculature (SynVA)**, a modular toolkit for the generation of anatomically plausible vascular meshes and subsequently evolving aneurysm geometries, following the physiological formation process in which aneurysms emerge from pre-existing vessel structures. SynVA supports both data-driven learning-based models and a model-driven procedural approach for synthesizing its two core components: healthy vessel structures and aneurysm geometries. The coupling between vessel generation and aneurysm formation is established via the selection of an ostium, defined as the intersection between the parent vessel and the aneurysm. This selection can be performed either manually for controlled generation of individual samples or automatically based on bifurcation regions or local curvature, enabling scalable large-scale dataset generation.

In summary, SynVA’s key contributions are as follows: **(1)** A flow matching-based healthy vessel generation model outperforming existing baselines; **(2)** Two methodologically distinct, ostium-conditioned learning-based models for localized aneurysm synthesis on existing vessels, building on AneuG [15] and MeshAnything V2 [10]; **(3)** A first of its kind procedural model for generating labeled vascular meshes and aneurysms based solely on biological and mathematical principles; **(4)** A large-scale synthetic dataset of 3D vessel structures with aneurysms comprising 50,000 samples.

## 2 Related work

**Procedural Vessel Generation** Prior work on procedural vascular modeling can be categorized into optimization-based tree synthesis, angiogenesis-based growth models, rule-based L-system approaches, and synthetic or application-driven generation for downstream imaging tasks. Optimization-based approaches minimize a hemodynamically motivated cost function. Most extend Constrained Constructive Optimization (CCO) with a local per-branch optimization [29, 35, 38, 76, 84], whereas

Jessen et al. [33] formulate it globally as a nonlinear program. Angiogenesis-based models instead simulate vascular growth as a response to diffusing biochemical signals, reproducing the biological mechanism rather than only its outcome [51, 75]. Rule-based and L-system-inspired methods provide procedural control over branching structure, guided by Murray-type assumptions and spatial constraints [24, 64, 67]. Synthetic approaches generate vascular structures for segmentation, pretraining, or aneurysm-detection tasks [3, 29, 56]. However, existing methods either focus on large-scale vascular trees without aneurysmal pathology [3, 29, 33, 35, 38, 51, 75, 76, 84], or model aneurysms only at the voxel/image level rather than as explicit, labeled mesh structures [56]. To our knowledge, no prior work produces fully procedural, high-resolution, explicitly labeled meshes of aneurysmal vessels.

**Mesh Generative AI** Early autoregressive methods such as PolyGen [57] model vertices and faces separately, while MeshGPT [78] introduces a tokenization-based approach, where triangle meshes are encoded into sequences of quantized latent embeddings. A transformer is then trained to autoregressively predict the next token, from which the full mesh can be decoded. This paradigm has been widely adopted and extended by subsequent works, often incorporating alternative architectures and conditioning mechanisms [7, 95, 96]. Beyond model design, recent research also focuses on improving mesh representations and tokenization strategies. For instance, MeshAnythingV2 [10] leverages an adjacent mesh tokenization (AMT) scheme to significantly increase the number of generatable faces from a given input point cloud, addressing a key limitation in high-resolution mesh synthesis. Other approaches explore specialized traversal and compression strategies to maximize representation efficiency [81, 85, 97]. More recent models such as MeshTron [30], DeepMesh [105], FastMesh [39], and MeshRipple [47] further advance mesh generation capabilities.

**Vascular Mesh Generation** Generative models for vascular structures can be broadly grouped into topology-oriented approaches, geometry-oriented approaches, and methods that explicitly separate global structure from local geometry. Early work such as VesselVAE [19] generates vascular trees from a hierarchical tree representation, but remains restricted to tree-like topologies and mainly captures coarse morphology through descriptors such as radius, length, and tortuosity. Subsequent topology-oriented methods extend this idea to more general structural representations [5, 41, 61]. However, these methods primarily operate at the level of structure, centerlines, or topology rather than directly modeling detailed surface geometry. In parallel, geometry-oriented methods focus on continuous shape representations. TrIND [80] models anatomical trees with implicit neural fields, while the semantic signed distance field approach of Kuipers et al. [42] directly generates surface representations of cerebral vascular trees. VesselGPT [20] further highlights the importance of local cross-sectional modeling through an autoregressive formulation based on B-spline cross-sections. Relatedly, Deo et al. [13] generate aneurysm-bearing vessel segmentations under few-shot conditions using latent diffusion with SDF-based conditioning. The closest work to our setting is the part-based model of Chen et al. [8], which decomposes generation into a global key-graph, local segment geometry, and assembly; VesselTok [62] similarly separates structural and geometric representation learning for vessel-like biomedical graphs. Nevertheless, existing methods either focus on structural generation without precise local surface control, or on continuous geometry without an equally explicit graph-based decomposition.

**Aneurysma Mesh Generation** Generative AI models for IA synthesis are motivated by the scarcity of large, high-quality annotated datasets and, more recently, by the need for simulation-ready aneurysm geometries for downstream hemodynamic analysis [13, 15, 16, 46]. Existing approaches mainly differ in whether they generate aneurysm-bearing segmentations, complete vascular geometries, or explicit 3D meshes. Deo et al. [13] propose a few-shot latent diffusion model for generating cerebral aneurysm geometries, producing aneurysm-bearing vessel segmentations with transformer-based class conditioning on anatomical locations and SDF-based shape conditioning. The closest methodological reference is AneuG [15], a two-stage VAE-based model that generates IA meshes by first synthesizing the aneurysm complex and then modeling the parent vessels conditioned on it, with additional control via morphological markers such as aspect ratio, neck width, lobulation index, and volume. Despite these advances, existing methods either generate aneurysm-bearing segmentations without direct surface-level control or synthesize complete aneurysm-parent-vessel complexes without explicitly modeling the ostium as the primary geometric constraint. This leaves a gap in modeling aneurysm formation as a localized, surface-consistent process on an existing healthy vessel mesh.

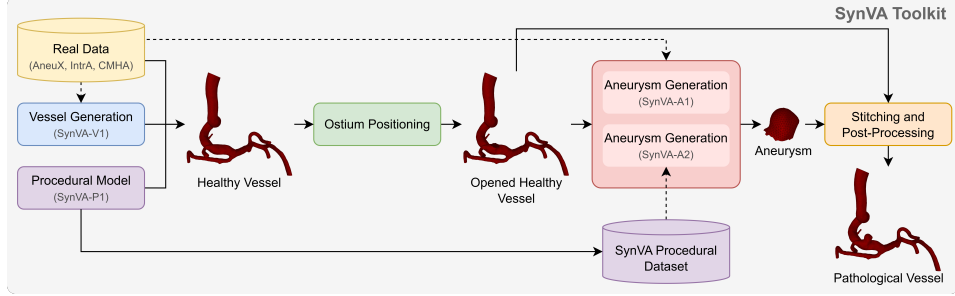


Figure 1: **Overview of the SynVA toolkit.** SynVA generates pathological vascular meshes by combining healthy vessel generation, ostium selection, and conditioned aneurysm synthesis. Healthy vessels are generated either with the two-stage flow-matching model SynVA-V1 or the procedural model SynVA-P1. An ostium is then selected on the vessel surface, either automatically based on bifurcation or curvature priors or manually for controlled editing. Conditioned on this ostium, aneurysms are generated using SynVA-A1, SynVA-A2, or SynVA-P1 and stitched to the parent vessel to obtain a complete labeled vessel–aneurysm mesh.

### 3 Methodology

SynVA is a modular toolkit (Fig. 1) for generating fully labeled 3D vascular meshes, including both healthy and pathological geometries with aneurysms. It integrates data-driven and model-driven paradigms within a unified toolkit. On the learning side, a flow matching–based model is used to learn the topology and geometry of healthy vascular structures (SynVA-V1). Additionally, we developed the SynVA-P1 procedural model for vessel structures based on physiological principles and statistical priors to generate vascular structures with and without aneurysms. A healthy vessel structure is used to select the position of an ostium – the ring around an aneurysm opening. We then use variants of AneuG [15] and MeshAnything V2 [10], referred to as SynVA-A1 and SynVA-A2, to generate aneurysm shapes conditioned on the ostium. In a post-processing step the generated aneurysm mesh is stitched onto the healthy vessel structure to generate a complete pathological vessel structure with an aneurysm. The following sections describe these components together with the associated interfaces for single-sample generation, editing, and large-scale dataset synthesis. The main focus of this work lies on the learning-based approaches, while the SynVA-P1 procedural model and the resulting synthetic dataset are detailed in Appx. G and H.

#### 3.1 SynVA-V1: Flow-matching based Vessel Generation

SynVA-V1 generates healthy vascular structures in a two-stage process. In the first stage, only the discrete vessel topology is learned as a rooted directed tree, whose edges encode the branching structure, without observing any continuous geometry. In the second stage, the sampled topology is held fixed and used as a structural condition for geometry generation. Given this tree, SynVA-V1 predicts continuous node features, including parent-relative centerline positions, local cross-section control points, and B-spline knot parameters. The generative model uses a topology-aware Graph Neural Network (GNN) [25] backbone that we refer to as *TreeFlowNet*. For each vessel tree, a multigraph is constructed with parent-to-child, child-to-parent, and sibling-to-sibling edges. Separate message-passing functions are used for the different edge types, enabling asymmetric information flow along anatomical directions. Local tree-based message passing is combined with alternating global self-attention, allowing the model to capture both nearby bifurcation structure and long-range dependencies between distant branches.

Training is performed using optimal-transport conditional flow matching [88] on the real dataset splits. Since all available real samples contain aneurysms, we derive healthy vessel data by manually removing aneurysmal regions through mesh sculpting operations, yielding anatomically plausible vessel-only reconstructions. Starting from Gaussian noise, the model learns a velocity field that transports noisy vessel geometries toward real vessel geometries while remaining conditioned on the fixed tree topology. The loss is computed over valid tree nodes and balances the position, cross-section, and spline-parameter components with separate weights. During inference, a new geometry is sampled by integrating the learned velocity field from noise to the data distribution.

Several refinements improve geometric realism and stability. A logit-normal time sampler emphasizes intermediate noise levels, while depth-warped time embeddings stabilize the generation of deeper branches. Focal position weighting increases the influence of small continuation steps along vessels, and optional auxiliary terms encourage plausible bifurcation geometry, sibling separation, radius decay, and cross-section consistency. After generation, the predicted node features are denormalized and converted into a spline-based vessel representation. The final healthy vessel mesh is reconstructed by sampling tubular point clouds along the spline segments and applying screened Poisson surface reconstruction with local smoothing at bifurcations. More details can be found in Appx. C.

### 3.2 SynVA-P1: Procedural Vessel Structure and Aneurysm Generation

SynVA-P1 is a procedural model for generating labeled pathological vascular meshes without relying on patient-specific input geometries. The model combines physiological constraints, statistical priors, and stochastic geometric perturbations. It generates a local bifurcating vessel configuration, optionally augmented with an aneurysm, through two stages: healthy vessel generation and aneurysm synthesis. First, a centerline representation of a bifurcating vessel is sampled. The parent diameter is drawn from a predefined range, while the child-branch diameters are derived according to Murray’s law, yielding physiologically plausible vessel proportions. A signed distance field is constructed around the centerlines and converted into a surface mesh using Marching Cubes. To avoid overly idealized tube-like shapes, the mesh is perturbed with multi-scale OpenSimplex noise, smoothed, cleaned, and isotropically remeshed. More details about the SynVA-P1 procedural model can be found in Appx. G.

### 3.3 Ostium Positioning

Ostium positioning can be performed either automatically (see Appx. G.2) or interactively via the graphical user interface in SynVA (manual ostium positioning, see Appx. D). The automatic approach ensures consistent and scalable placement driven by geometric priors and statistically informed hemodynamic assumptions, making it well suited for large-scale data generation. In contrast, the manual approach enables precise specification, refinement, and cropping of the ostium, which is particularly useful for single-sample generation and targeted editing of existing vessel geometries. In automatic ostium selection, two complementary strategies are employed. For bifurcation-based placement, the junction is identified from the centerline topology, and the local flow direction of the parent vessel is approximated from nearby centerline tangents. Within a local neighborhood, surface vertices are evaluated using APSS-based curvature estimation [27, 28], and the ostium is defined as the minimally curved vertex aligned with the flow direction. This choice is motivated by the increased hemodynamic stress typically observed in this region, which has been strongly associated with aneurysm formation [22, 66, 72]. For curvature-based placement, a curvature score is computed along the centerline to identify high-curvature regions. Surface vertices in the corresponding neighborhood are then evaluated, and the ostium is selected at either maximal (dominant case) or minimal curvature, capturing both outward- and inward-facing configurations observed in clinical data. Further details are provided in Appx. G.2.

### 3.4 Ostium-Conditioned Aneurysm Generation

Aneurysm synthesis in SynVA is formulated as a localized, anatomy-conditioned generation task. Instead of generating aneurysms as isolated objects or complete aneurysm–vessel complexes, all three aneurysm generators operate on a predefined ostium on an existing healthy vessel surface. The ostium defines the attachment boundary, local scale, and growth direction of the aneurysm. This formulation reflects the physiological setting in which aneurysms emerge from pre-existing vascular structures and ensures that the generated geometry can be consistently stitched back onto the parent vessel. We consider three complementary approaches for conditioned aneurysm generation: two learning-based models, SynVA-A1 and SynVA-A2, and the procedural model SynVA-P1.

**SynVA-A1** builds on AneuG [15] and uses a compact GHD-based latent representation of aneurysm morphology. In contrast to the original configuration, where aneurysm and parent-vessel geometry are modeled jointly in a two-stage generative process, we adapt the formulation to focus on the aneurysm sac and neck region conditioned on the local ostium geometry. This allows the model to synthesize aneurysm shapes as localized deformations anchored to the vessel surface, while the surrounding healthy vasculature is provided by the input vessel mesh. To enable this formulation,



Figure 2: Example generated vessel geometries conditioned on the ground-truth topology.

we condition not only on independent morphological parameters but additionally on the explicit ostium ring geometry, dense samples from the segmented ostium attachment region, compact ostium parameters, and local vessel structure. Furthermore, dedicated loss terms that enforce geometric consistency at the vessel–aneurysm interface are introduced, including consistency with the ostium attachment region, the opening center, and the expected side of the ostium plane. In addition to the standard posterior reconstruction path of the conditional VAE, we explicitly regularize the prior sampling path by decoding samples from  $z \sim \mathcal{N}(0, I)$  under the same condition and matching them to case-level and batch-level target statistics. The generated aneurysm is subsequently transformed back into the vessel coordinate system and merged with the parent vessel at the ostium. More details can be found in Appx. E.

**SynVA-A2** extends MeshAnything V2 [10] from full-shape mesh reconstruction to ostium-conditioned autoregressive aneurysm generation. Since the complete aneurysm geometry is not available at inference time, the model is conditioned only on partial anatomical context: a local vessel point cloud around the ostium and an explicit ostium mesh. The local point cloud provides geometric context about the parent vessel, while the ostium mesh is tokenized and injected as a forced prefix into the autoregressive sequence. The transformer therefore starts generation from the correct anatomical boundary and predicts the aneurysm mesh as a continuation of the ostium, rather than reconstructing a complete object from a full point cloud. During training, the sequence consists of the ostium prefix followed by the aneurysm continuation, with the loss applied only to the generated aneurysm tokens. More details can be found in Appx. F.

**SynVA-P1** provides a procedural model alternative that does not rely on learned shape priors. Given the ostium centroid, ostium normal, and local vessel radius, the aneurysm sac is initialized from a simple geometric primitive, scaled to the vessel size, elongated along the ostium normal, and perturbed with stochastic surface noise to introduce shape variability. Optionally, a secondary protrusion is added to simulate bleb-like irregularities. The resulting aneurysm mesh is merged with the healthy vessel using mesh boolean operations, followed by remeshing, smoothing, and relabeling. More details can be found in Appx. G.

For all three approaches, the final step is a post-processing and stitching procedure. Invalid or degenerate mesh elements are removed, normals are recomputed, and the aneurysm is aligned with the ostium in the original vessel coordinate frame. The aneurysm and vessel meshes are then merged at the ostium interface, and the transition region is smoothed to obtain a single pathological vascular mesh. The final output contains a complete surface representation with semantic labels for healthy vessel, aneurysm, and ostium regions, enabling downstream use in segmentation, morphology analysis, and simulation-oriented workflows.

### 3.5 Data and Pre-Processing

We utilize a total of 769 samples from three publicly available datasets containing vascular meshes and IAs. Due to differences in data acquisition, preprocessing pipelines, and mesh representations, each dataset is processed independently to obtain a consistent representation of complete vessels with per-vertex labels. A unified preprocessing pipeline is then applied across all datasets to ensure consistency. This includes normalization of mesh coordinates to the range  $[-1, 1]$ , extraction of labeled point clouds and corresponding sub-point clouds, computation of the ostium centroid and its

associated normal vector (oriented toward the aneurysm), sub-mesh extraction, and the computation of relevant morphological parameters (see Appx. B). All processed data are stored in a unified and standardized data structure, comprising full meshes, vertex-wise labels, (sub-)point clouds, (sub-)meshes, and additional attributes such as morphological descriptors (see Appx. B and G). Primarily this project uses data from the AneuX morphology database [34], an open-access, multi-centric database combining data from three European projects: AneuX project, @neurIST project [32, 92] and Aneurisk [71]. It constitutes the largest dataset in our study, comprising 605 patients, 668 vessel trees, and 750 aneurysm meshes with varying cut configurations and mesh resolutions. In addition, clinical and morphological metadata are provided. We use the original mesh resolution and the dome cut configuration (resulting in 564 samples). Following a qualitative inspection, 6 samples were excluded, resulting in a total of 558 samples used in our experiments. The second dataset is the Intracranial Aneurysm Dataset for Deep Learning (IntrA) [102], which contains 103 full cerebrovascular models. In addition to automatically generated segmentation meshes, the dataset provides 116 manually annotated segments. After excluding one sample with more than one aneurysm, the remaining annotated segments are incorporated into our standardized data representation. The third dataset is the CMHA dataset [82], which includes 99 patients with aneurysms and 44 control subjects, along with morphological and hemodynamic parameters. From this dataset, we use 96 aneurysm cases, excluding three samples with more than one ostium ring.

In addition to the real-world datasets, we generate a large-scale synthetic dataset using the SynVA-P1 procedural model (see Appx. H). In total, SynVA-P1 is used to create 50,000 pathological vascular meshes with aneurysms. Each sample is generated independently by sampling a bifurcating vessel geometry, selecting an ostium according to the procedural placement strategy, synthesizing an aneurysm sac conditioned on the ostium location, normal direction, and local vessel radius, and finally stitching the aneurysm to the vessel surface. The same preprocessing used for the real data is then applied to the synthetic samples. Consequently, each synthetic datapoint contains a complete pathological vessel mesh with vertex-wise labels for vessel, aneurysm, and ostium regions, as well as derived point clouds, submeshes, centerline and radius information, ostium descriptors, and morphological parameters.

## 4 Experiments and Results

For all experiments, we use consistent train–test splits across models to prevent data leakage. For real data, 100 samples are selected as a stratified test set across the three individual datasets. For the synthetic dataset, 10,000 samples are randomly held out for testing. All experiments for the three learning-based models (SynVA-V1, SynVA-A1, and SynVA-A2) are conducted on a system with 2× NVIDIA B200 GPUs (180 GB VRAM each) and 16× Intel Xeon Platinum 8570 CPUs (56 cores each), running Ubuntu 24.04.

### 4.1 Healthy Vessel Generation (SynVA-V1)

We evaluate SynVA-V1 with geometry metrics (Maximum Mean Discrepancy (MMD) [26], Coverage (COV) [1], 1-Nearest-Neighbor Accuracy (1-NNA) [49] on a 13-dimensional per-tree feature vector, the radius-histogram cosine similarity  $\text{cos}_{\text{radius}}$  [19]), topology metrics ( $\text{KL}_{\text{degree}}$  on the node-degree distribution, and the Laplacian-spectrum distance Spec. [8]), benchmarking against VesselGPT [20] and VesselVAE [19] as the most recent established baselines. Since centerline extraction failed for 40 out of 100 manually curated test-split ground-truth samples of healthy vessels, we restrict our evaluation to a subset of  $n = 60$  successfully processed samples. All literature values in Tab. 1 are quoted verbatim from the cited works on their original datasets.

Because each baseline was evaluated on a different dataset, the comparison is indicative rather than strict. With this caveat, our three geometry variants achieve numerically better values than VesselGPT on all metrics it reports, while VesselVAE’s published MMD on IntrA is lower than ours on our test set; on COV, 1-NNA and  $\text{cos}_{\text{radius}}$  our best variant remains ahead of the VesselVAE numbers. SynVA-V1<sub>topology</sub> reports lower  $\text{KL}_{\text{degree}}$  and Spec. values than the cited sources, again under the cross-dataset caveat. Qualitative samples (Fig. 2) confirm that the geometry variants generate both short and long vessel sequences under ground-truth topology while preserving meaningful geometric variability; further analyses (t-SNE, per-variant ablations) are deferred to Appx. C.

Table 1: SynVA-V1 vs. published vessel-generation methods. *Upper block*: our three geometry variants and SynVA-V1<sub>topology</sub> evaluated on a curated  $n=60$  test subset<sup>†</sup> of AneuX [34], IntrA [102] and the CMHA[82] dataset. *Lower block*: literature values quoted verbatim from the cited works on their respective source datasets.

| Method                       | Dataset                       | MMD↓         | COV↑         | 1-NNA→.5     | cosradius ↑  | KL-degree ↓   | Spec.↓        |
|------------------------------|-------------------------------|--------------|--------------|--------------|--------------|---------------|---------------|
| SynVA-V1 <sub>base</sub>     | AneuX+IntrA+CMHA <sup>†</sup> | 0.042        | <b>0.500</b> | 0.725        | 0.970        | —             | —             |
| SynVA-V1 <sub>depth</sub>    | AneuX+IntrA+CMHA <sup>†</sup> | 0.040        | 0.483        | 0.717        | <b>0.974</b> | —             | —             |
| SynVA-V1 <sub>aligned</sub>  | AneuX+IntrA+CMHA <sup>†</sup> | 0.077        | 0.433        | <b>0.700</b> | 0.950        | —             | —             |
| SynVA-V1 <sub>topology</sub> | AneuX+IntrA+CMHA <sup>†</sup> | —            | —            | —            | —            | <b>0.0013</b> | <b>0.0008</b> |
| VesselGPT [20]               | IntrA                         | 0.140        | 0.410        | 0.170        | —            | —             | —             |
| VesselVAE [19]               | IntrA                         | <b>0.013</b> | 0.450        | 0.126        | 0.970        | —             | —             |
| Prabhakar et al. [61]        | VesSAP [59, 87]               | —            | —            | —            | —            | 0.006         | —             |
| Prabhakar et al. [61]        | CoW [101]                     | —            | —            | —            | —            | 0.003         | —             |
| Chen et al. [8]              | ImageCAS [103]                | —            | —            | —            | —            | 0.601         | 0.079         |
| Chen et al. [8]              | VascuSynth [29]               | —            | —            | —            | —            | 0.190         | 0.159         |
| Chen et al. [8]              | CoW [101]                     | —            | —            | —            | —            | 1.475         | 0.182         |

Table 2: Quantitative comparison of SynVA-A1 and SynVA-A2 on the aneurysm test set. For a fair comparison, results are also shown on the subset of SynVA-A2 successful generations ( $n = 66$ ).

| Mean Absolute Difference | SynVA-A1 ( $N = 100$ ) | SynVA-A1 ( $n = 66$ )  | SynVA-A2 ( $n = 66$ ) |
|--------------------------|------------------------|------------------------|-----------------------|
| $A_A$                    | 0.1560 ± 0.2599        | <b>0.1634 ± 0.2853</b> | 0.1963 ± 0.3248       |
| $A_{CH}$                 | 0.1539 ± 0.2631        | <b>0.1606 ± 0.2850</b> | 0.1986 ± 0.3238       |
| $D_{max}$                | 0.0842 ± 0.0992        | <b>0.0866 ± 0.1034</b> | 0.1028 ± 0.1085       |
| $H_{max}$                | 0.0796 ± 0.0905        | <b>0.0826 ± 0.0962</b> | 0.1100 ± 0.1116       |
| $H_{ortho}$              | 0.0715 ± 0.0821        | <b>0.0764 ± 0.0906</b> | 0.1035 ± 0.0975       |
| $V_A$                    | 0.0214 ± 0.0449        | <b>0.0224 ± 0.0486</b> | 0.0330 ± 0.0608       |
| $V_{CH}$                 | 0.0214 ± 0.0449        | <b>0.0224 ± 0.0486</b> | 0.0257 ± 0.0553       |
| $W_{max}$                | 0.0574 ± 0.0805        | <b>0.0581 ± 0.0856</b> | 0.0694 ± 0.0927       |
| $W_{ortho}$              | 0.0567 ± 0.0752        | <b>0.0572 ± 0.0798</b> | 0.0703 ± 0.0895       |
| Chamfer Distance         | 0.0864 ± 0.0652        | <b>0.0919 ± 0.0695</b> | 0.1001 ± 0.0710       |

## 4.2 Aneurysm Generation and Pathological Vessels (SynVA-A1, SynVA-A2)

To evaluate the two ostium-conditioned learning-based models, SynVA-A1 and SynVA-A2, we report results for their respective best-performing configurations, selected from extensive experiments exploring architectural choices, training strategies, and data settings (details provided in Appx. E and F). The quantitative comparison is based on the mean absolute differences of independent morphological parameters and the Chamfer distance on the test set, enabling a precise assessment of shape fidelity. Results in Tab. 2 show that SynVA-A1 performs slightly better on the shared subset of successful generations from SynVA-A2 (success rate of 66%), yielding lower parameter deviations and a reduced Chamfer distance.

The quantitative results are complemented by an expert study involving two neuroradiologists. For 40 real vessel cases, each expert was presented with the corresponding ground-truth aneurysm as well as aneurysms generated by SynVA-A1 and SynVA-A2 side by side, resulting in 120 evaluated samples. All aneurysms were generated at the same ostium of the respective vessel. The experts rated each pathological vessel on a scale from 0 (unrealistic) to 5 (realistic), without being informed which samples were ground truth or model-generated, to avoid systematic bias.

The mean ratings (Tab. 3) show that ground-truth aneurysms are, on average, perceived as most realistic. Among the generated samples, SynVA-A2 is rated slightly higher than SynVA-A1, although the differences remain marginal. Qualitative feedback from the experts indicates that overly symmetric shapes, irregular proportions between aneurysm neck and sac, and sharp geometric artifacts reduce perceived realism. Interestingly, certain ground-truth samples—particularly aneurysms with pronounced flask-neck morphologies—were also rated as less realistic, which may indicate potential labeling inconsistencies in the real dataset. Qualitative examples are shown in Fig. 3. Both models consistently generate aneurysms conditioned on the ostium and the local vessel geometry, producing shapes that closely resemble the ground truth while still exhibiting plausible anatomical variation. Neither model is visually dominant: both produce comparable results, with only minor differences, consistent with the quantitative metrics and expert ratings.

Table 3: Medical expert evaluation of aneurysm realism on a scale from 0 to 5 across  $n = 40$  cases.

|                  | GT ( $n = 40$ )                     | SynVA-A1 ( $n = 40$ ) | SynVA-A2 ( $n = 40$ ) |
|------------------|-------------------------------------|-----------------------|-----------------------|
| Medical Expert 1 | $4.675 \pm 0.797$                   | $4.500 \pm 0.751$     | $4.475 \pm 0.640$     |
| Medical Expert 2 | $4.350 \pm 1.051$                   | $3.550 \pm 1.011$     | $3.950 \pm 0.783$     |
| Combined Rating  | <b><math>4.513 \pm 0.941</math></b> | $4.025 \pm 1.006$     | $4.213 \pm 0.758$     |

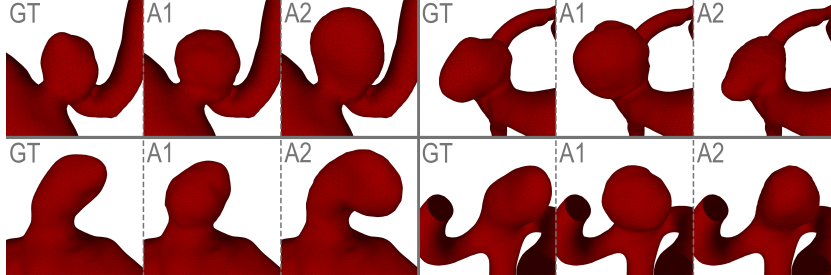


Figure 3: Qualitative comparison of ground-truth and generated aneurysms on real vessel geometries.

## 5 Discussion

SynVA demonstrates how learning-based and procedural generation can be combined to synthesize labeled vascular meshes with anatomy-conditioned aneurysms. A central design choice is to decouple healthy vessel generation from aneurysm synthesis and to connect both through an explicit ostium. This formulation reflects aneurysm formation as a localized process on a pre-existing vessel surface, while enabling both scalable automatic generation and controlled editing. For healthy vessel generation, SynVA-V1 shows strong performance across both topology and geometry. The topology component outperforms prior methods, while the geometry models achieve competitive or superior results in most metrics. Although direct numerical comparison is limited due to differing datasets and evaluation protocols, both quantitative metrics and qualitative examples indicate that the proposed models generate realistic and consistent vascular structures. Minor artifacts, such as occasional circular patterns in mesh reconstruction, are rare and have negligible impact. The procedural variant SynVA-P1 provides a robust and fully controllable alternative, but is currently limited in complexity, as it supports only a single bifurcation. The aneurysm generators exhibit complementary strengths. SynVA-A1 reliably approximates ground-truth shapes and achieves stronger quantitative performance, benefiting from richer conditioning signals. However, it tends to produce slightly more symmetric geometries, which can reduce perceived realism. In contrast, SynVA-A2 generates more clinically plausible shapes according to expert assessment, despite weaker quantitative metrics and a higher failure rate in mesh generation. This highlights that improved numerical accuracy does not necessarily translate to higher clinical realism. Overall, both learning-based models produce plausible aneurysms conditioned on local vessel anatomy, while the procedural approach SynVA-P1 offers controllability at the cost of reduced variability due to its limited conditioning.

## 6 Conclusion, Limitations and Future Work

We presented SynVA, a modular toolkit for synthetic vascular mesh generation and anatomy-conditioned aneurysm synthesis. SynVA combines a two-stage flow-matching model for healthy vessel generation, ostium-conditioned learning-based aneurysm generators, and a fully procedural model for scalable data synthesis. By generating aneurysms from a predefined ostium on an existing vessel surface, SynVA models aneurysm formation as a localized, vessel-conditioned process rather than as isolated shape generation. The resulting pipeline produces complete pathological vascular meshes with semantic labels, morphological descriptors, and consistent vessel-aneurysm interfaces, including a large-scale synthetic dataset of 50,000 samples which enabled the training of our SynVA-A1 model. SynVA has several limitations. The current vessel model focuses on local tree-like structures and does not yet capture complete patient-level cerebrovascular anatomy or all variants of the Circle of Willis. The procedural component relies on simplified physiological assumptions and statistical priors, while the learning-based models inherit biases from heterogeneous and limited real aneurysm datasets. In addition, the generated geometries are optimized for anatomical and morphological plausibility, but hemodynamic quantities such as wall shear stress or pressure

fields are not explicitly modeled. Some meshes may therefore require further preparation before CFD-based analysis. Future work will extend SynVA toward larger and more anatomically complete vascular networks, incorporate vessel-type and location-specific priors, and condition aneurysm generation on hemodynamic or simulation-derived descriptors. We also plan to evaluate the utility of SynVA-generated data in additional downstream tasks such as segmentation, morphology-based risk assessment, and accelerated flow prediction.

### **Acknowledgments and Disclosure of Funding**

This work was supported by the IDIR-Project (Digital Implant Research), a cooperation financed by Kiel University, University Hospital Schleswig-Holstein and Helmholtz Zentrum Hereon.

## References

- [1] Panos Achlioptas, Olga Diamanti, Ioannis Mitliagkas, and Leonidas Guibas. Learning representations and generative models for 3d point clouds. In *International conference on machine learning*, pages 40–49. PMLR, 2018.
- [2] Dieuwertje Alblas, Christoph Brune, and Jelmer M Wolterink. Deep-learning-based carotid artery vessel wall segmentation in black-blood mri using anatomical priors. In *Medical Imaging 2022: Image Processing*, volume 12032, pages 237–244. SPIE, 2022.
- [3] Nil Stolt Ansó. Synthetic vascular structure generation for unsupervised pre-training in cta segmentation tasks. *arXiv preprint arXiv:2001.00666*, 2020.
- [4] Luca Antiga, Marina Piccinelli, Lorenzo Botti, Bogdan Ene-Iordache, Andrea Remuzzi, and David A Steinman. An image-based modeling framework for patient-specific computational hemodynamics. *Medical & biological engineering & computing*, 46(11):1097–1112, 2008.
- [5] James Batten, Michiel Schaap, Matthew Sinclair, Ying Bai, and Ben Glocker. Vector representations of vessel trees. *arXiv preprint arXiv:2506.11163*, 2025.
- [6] Brain Aneurysm Foundation. Statistics and facts. <https://www.bafound.org/understanding-brain-aneurysms/statistics-and-facts/>, 2026. Accessed: 2026-04-15.
- [7] Sijin Chen, Xin Chen, Anqi Pang, Xianfang Zeng, Wei Cheng, Yijun Fu, Fukun Yin, Zhibin Wang, Jingyi Yu, Gang Yu, et al. Meshxl: Neural coordinate field for generative 3d foundation models. *Advances in Neural Information Processing Systems*, 37:97141–97166, 2024.
- [8] Siqi Chen, Guoqing Zhang, Jiahao Lai, Bingzhi Shen, Sihong Zhang, Caixia Dong, Xuejin Chen, and Yang Li. Hierarchical part-based generative model for realistic 3d blood vessel. In *International Conference on Medical Image Computing and Computer-Assisted Intervention*, pages 257–267. Springer, 2025.
- [9] Yiwen Chen, Tong He, Di Huang, Weicai Ye, Sijin Chen, Jiayang Tang, Xin Chen, Zhonggang Cai, Lei Yang, Gang Yu, et al. Meshanything: Artist-created mesh generation with autoregressive transformers. *arXiv preprint arXiv:2406.10163*, 2024.
- [10] Yiwen Chen, Yikai Wang, Yihao Luo, Zhengyi Wang, Zilong Chen, Jun Zhu, Chi Zhang, and Guosheng Lin. Meshanything v2: Artist-created mesh generation with adjacent mesh tokenization. In *Proceedings of the IEEE/CVF International Conference on Computer Vision*, pages 13922–13931, 2025.
- [11] Chloe M de Nys, Ee Shern Liang, Marita Prior, Maria A Woodruff, James I Novak, Ashley R Murphy, Zhiyong Li, Craig D Winter, and Mark C Allenby. time-of-flight mra of intracranial aneurysms with interval surveillance, clinical segmentation and annotations. *Scientific Data*, 11(1):555, 2024.
- [12] Méghane Decroocq, Carole Frindel, Pierre Rougé, Makoto Ohta, and Guillaume Lavoué. Modeling and hexahedral meshing of cerebral arterial networks from centerlines. *Medical image analysis*, 89:102912, 2023.
- [13] Yash Deo, Fengming Lin, Haoran Dou, Nina Cheng, Nishant Ravikumar, Alejandro F Frangi, and Toni Lassila. Few-shot learning in diffusion models for generating cerebral aneurysm geometries. In *2024 IEEE International Symposium on Biomedical Imaging (ISBI)*, pages 1–5. IEEE, 2024.
- [14] Sujan Dhar, Markus Tremmel, J Mocco, Minsuok Kim, Junichi Yamamoto, Adnan H Siddiqui, L Nelson Hopkins, and Hui Meng. Morphology parameters for intracranial aneurysm rupture risk assessment. *Neurosurgery*, 63(2):185–197, 2008.
- [15] Wenhao Ding, Kangjun Ji, Simão Castro, Yihao Luo, Dylan Roi, and Choon Hwai Yap. Two-stage generative model for intracranial aneurysm meshes with morphological marker conditioning. In *International Conference on Medical Image Computing and Computer-Assisted Intervention*, pages 595–604. Springer, 2025.

- [16] Wenhao Ding, Yiyang Sheng, Simão Nieto de Castro, Hwa Liang Leo, and Choon Hwai Yap. Aneug-flow: A large-scale synthetic dataset of diverse intracranial aneurysm geometries and hemodynamics. In *The Thirty-ninth Annual Conference on Neural Information Processing Systems Datasets and Benchmarks Track*, 2025.
- [17] Tolga Erol, Arif Furkan Mendi, and Dilara Doğan. The digital twin revolution in healthcare. In *2020 4th international symposium on multidisciplinary studies and innovative technologies (ISMSIT)*, pages 1–7. IEEE, 2020.
- [18] Patrick Esser, Sumith Kulal, Andreas Blattmann, Rahim Entezari, Jonas Müller, Harry Saini, Yam Levi, Dominik Lorenz, Axel Sauer, Frederic Boesel, Dustin Podell, Tim Dockhorn, Zion English, Kyle Lacey, Alex Goodwin, Yannik Marek, and Robin Rombach. Scaling rectified flow transformers for high-resolution image synthesis. In *International Conference on Machine Learning (ICML)*, 2024.
- [19] Paula Feldman, Miguel Fainstein, Viviana Siless, Claudio Delrieux, and Emmanuel Iarussi. Vesselvae: Recursive variational autoencoders for 3d blood vessel synthesis. In *International Conference on Medical Image Computing and Computer-Assisted Intervention*, pages 67–76. Springer, 2023.
- [20] Paula Feldman, Martin Sinnona, Claudio Delrieux, Viviana Siless, and Emmanuel Iarussi. Vesselgpt: Autoregressive modeling of vascular geometry. In *International Conference on Medical Image Computing and Computer-Assisted Intervention*, pages 662–672. Springer, 2025.
- [21] Robert W Floyd. Algorithm 97: shortest path. *Communications of the ACM*, 5(6):345–345, 1962.
- [22] Michael Forsting, Isabel Wanke, et al. *Intracranial vascular malformations and aneurysms*. Springer, 2006.
- [23] Juhana Frösen, Riikka Tulamo, Anders Paetau, Elisa Laaksamo, Miikka Korja, Aki Laakso, Mika Niemelä, and Juha Hernesniemi. Saccular intracranial aneurysm: pathology and mechanisms. *Acta neuropathologica*, 123(6):773–786, 2012.
- [24] Miguel A Galarreta-Valverde, Maysa MG Macedo, Choukri Mekkaoui, and Marcel P Jackowski. Three-dimensional synthetic blood vessel generation using stochastic l-systems. In *Medical Imaging 2013: Image Processing*, volume 8669, pages 414–419. SPIE, 2013.
- [25] Justin Gilmer, Samuel S Schoenholz, Patrick F Riley, Oriol Vinyals, and George E Dahl. Neural message passing for quantum chemistry. In *International conference on machine learning*, pages 1263–1272. Pmlr, 2017.
- [26] Arthur Gretton, Karsten M Borgwardt, Malte J Rasch, Bernhard Schölkopf, and Alexander Smola. A kernel two-sample test. *The journal of machine learning research*, 13(1):723–773, 2012.
- [27] Gaël Guennebaud and Markus Gross. Algebraic point set surfaces. In *ACM siggraph 2007 papers*, pages 23–es. 2007.
- [28] Gaël Guennebaud, Marcel Germann, and Markus Gross. Dynamic sampling and rendering of algebraic point set surfaces. In *Computer Graphics Forum*, volume 27, pages 653–662. Wiley Online Library, 2008.
- [29] Ghassan Hamarneh and Preet Jassi. Vascusynth: Simulating vascular trees for generating volumetric image data with ground-truth segmentation and tree analysis. *Computerized medical imaging and graphics*, 34(8):605–616, 2010.
- [30] Zekun Hao, David W Romero, Tsung-Yi Lin, and Ming-Yu Liu. Meshtron: High-fidelity, artist-like 3d mesh generation at scale. *arXiv preprint arXiv:2412.09548*, 2024.
- [31] Hugues Hoppe, Tony DeRose, Tom Duchamp, John McDonald, and Werner Stuetzle. Mesh optimization. In *Proceedings of the 20th annual conference on Computer graphics and interactive techniques*, pages 19–26, 1993.

- [32] Jimison Iavindrasana, Luigi Lo Iacono, Henning Müller, Ivan Periz, Paul Summers, Jessica Wright, Christoph M Friedrich, Holger Dach, Tobias Gattermayer, Gerhard Engelbrecht, et al. The@ neurist project. *Studies in health technology and informatics*, 138:161–164, 2008.
- [33] Etienne Jessen, Marc C Steinbach, and Dominik Schillinger. Optimizing non-intersecting synthetic vascular trees in nonconvex organs. *IEEE Transactions on Biomedical Engineering*, 2025.
- [34] Norman Juchler, Sabine Schilling, Philippe Bijlenga, Vartan Kurtcuoglu, and Sven Hirsch. Shape trumps size: image-based morphological analysis reveals that the 3d shape discriminates intracranial aneurysm disease status better than aneurysm size. *Frontiers in neurology*, 13: 809391, 2022.
- [35] Rudolf Karch, Friederike Neumann, Martin Neumann, and Wolfgang Schreiner. Staged growth of optimized arterial model trees. *Annals of biomedical engineering*, 28(5):495–511, 2000.
- [36] Michael Kazhdan and Hugues Hoppe. Screened poisson surface reconstruction. *ACM Transactions on Graphics (ToG)*, 32(3):1–13, 2013.
- [37] Alexander Keedy. An overview of intracranial aneurysms. *McGill Journal of Medicine: MJM*, 9(2):141, 2006.
- [38] Hyun Jin Kim, Hans Christian Rundfeldt, Inpyo Lee, and Seungmin Lee. Tissue-growth-based synthetic tree generation and perfusion simulation. *Biomechanics and Modeling in Mechanobiology*, 22(3):1095–1112, 2023.
- [39] Jeonghwan Kim, Yushi Lan, Armando Fortes, Yongwei Chen, and Xingang Pan. Fastmesh: Efficient artistic mesh generation via component decoupling. *arXiv preprint arXiv:2508.19188*, 2025.
- [40] Harold W Kuhn. The hungarian method for the assignment problem. *Naval research logistics quarterly*, 2(1-2):83–97, 1955.
- [41] Thijs P Kuipers, Praneeta R Konduri, Henk Marquering, and Erik J Bekkers. Generating cerebral vessel trees of acute ischemic stroke patients using conditional set-diffusion. In *Medical Imaging with Deep Learning*, 2024.
- [42] Thijs P Kuipers, Praneeta R Konduri, Erik J Bekkers, and Henk Marquering. Self-supervised synthetic cerebral vessel tree generation using semantic signed distance fields. In *Medical Imaging with Deep Learning*, 2025.
- [43] Hongzhi Lan, Adam Updegrave, Nathan M Wilson, Gabriel D Maher, Shawn C Shadden, and Alison L Marsden. A re-engineered software interface and workflow for the open-source simvascular cardiovascular modeling package. *Journal of biomechanical engineering*, 140(2): 024501, 2018.
- [44] Jung Yeop Lee and Sang Joon Lee. Murray’s law and the bifurcation angle in the arterial micro-circulation system and their application to the design of microfluidics. *Microfluidics and nanofluidics*, 8(1):85–95, 2010.
- [45] Gaoyang Li, Haoran Wang, Mingzi Zhang, Simon Tupin, Aike Qiao, Youjun Liu, Makoto Ohta, and Hitomi Anzai. Prediction of 3d cardiovascular hemodynamics before and after coronary artery bypass surgery via deep learning. *Communications biology*, 4(1):99, 2021.
- [46] Xigui Li, Yuanye Zhou, Feiyang Xiao, Xin Guo, Chen Jiang, Tan Pan, Xingmeng Zhang, Cenyu Liu, Zeyun Miao, Jianchao Ge, et al. Aneumo: A large-scale multimodal aneurysm dataset with computational fluid dynamics simulations and deep learning benchmarks. *arXiv preprint arXiv:2505.14717*, 2025.
- [47] Junkai Lin, Hang Long, Huipeng Guo, Jielei Zhang, JiaYi Yang, Tianle Guo, Yang Yang, Jianwen Li, Wenxiao Zhang, Matthias Nießner, et al. Meshripple: Structured autoregressive generation of artist-meshes. *arXiv preprint arXiv:2512.07514*, 2025.

- [48] Yaron Lipman, Ricky TQ Chen, Heli Ben-Hamu, Maximilian Nickel, and Matt Le. Flow matching for generative modeling. *arXiv preprint arXiv:2210.02747*, 2022.
- [49] David Lopez-Paz and Maxime Oquab. Revisiting classifier two-sample tests. *arXiv preprint arXiv:1610.06545*, 2016.
- [50] William E Lorensen and Harvey E Cline. Marching cubes: A high resolution 3d surface construction algorithm. In *Seminal graphics: pioneering efforts that shaped the field*, pages 347–353. 1998.
- [51] Florian Milde, Michael Bergdorf, and Petros Koumoutsakos. A hybrid model for three-dimensional simulations of sprouting angiogenesis. *Biophysical journal*, 95(7):3146–3160, 2008.
- [52] J Mocco, Robert D Brown Jr, James C Torner, Ana W Capuano, Kyle M Fargen, Madhavan L Raghavan, David G Piepgras, Irene Meissner, John Huston III, and International Study of Unruptured Intracranial Aneurysms Investigators. Aneurysm morphology and prediction of rupture: an international study of unruptured intracranial aneurysms analysis. *Neurosurgery*, 82(4):491–496, 2018.
- [53] Lei Mou, Jinghui Lin, Yifan Zhao, Yonghuai Liu, Shaodong Ma, Jiong Zhang, Wenhao Lv, Tao Zhou, Alejandro F Frangi, and Yitian Zhao. Costa: A multi-center multi-vendor tof-mra dataset and a novel cerebrovascular segmentation network. *IEEE Trans. Med. Imaging*, 2024.
- [54] Cecil D Murray. The physiological principle of minimum work: I. the vascular system and the cost of blood volume. *Proceedings of the National Academy of Sciences*, 12(3):207–214, 1926.
- [55] Cecil D Murray. The physiological principle of minimum work applied to the angle of branching of arteries. *The Journal of general physiology*, 9(6):835, 1926.
- [56] Rafic Nader, Florent Autrusseau, Vincent L’allicec, and Romain Bourcier. Building a synthetic vascular model: Evaluation in an intracranial aneurysms detection scenario. *IEEE Transactions on Medical Imaging*, 44(3):1347–1358, 2024.
- [57] Charlie Nash, Yaroslav Ganin, SM Ali Eslami, and Peter Battaglia. Polygen: An autoregressive generative model of 3d meshes. In *International conference on machine learning*, pages 7220–7229. PMLR, 2020.
- [58] Uli Niemann, Philipp Berg, Annika Niemann, Oliver Beuing, Bernhard Preim, Myra Spiliopoulou, and Sylvia Saalfeld. Rupture status classification of intracranial aneurysms using morphological parameters. In *2018 IEEE 31st International Symposium on Computer-Based Medical Systems (CBMS)*, pages 48–53. IEEE, 2018.
- [59] Johannes C Paetzold, Julian McGinnis, Suprosanna Shit, Ivan Ezhov, Paul Büschl, Chinmay Prabhakar, Mihail I Todorov, Anjany Sekuboyina, Georgios Kaissis, Ali Ertürk, et al. Whole brain vessel graphs: a dataset and benchmark for graph learning and neuroscience (vesselgraph). *arXiv preprint arXiv:2108.13233*, 2021.
- [60] Pointcept Contributors. Pointcept: A codebase for point cloud perception research. <https://github.com/Pointcept/Pointcept>, 2023.
- [61] Chinmay Prabhakar, Suprosanna Shit, Fabio Musio, Kaiyuan Yang, Tamaz Amiranashvili, Johannes C Paetzold, Hongwei Bran Li, and Bjoern Menze. 3d vessel graph generation using denoising diffusion. In *International Conference on Medical Image Computing and Computer-Assisted Intervention*, pages 3–13. Springer, 2024.
- [62] Chinmay Prabhakar, Bastian Wittmann, Tamaz Amiranashvili, Paul Büschl, Ezequiel de la Rosa, Julian McGinnis, Benedikt Wiestler, Bjoern Menze, and Suprosanna Shit. VesselTok: Tokenizing vessel-like 3d biomedical graph representations for reconstruction and generation. *arXiv preprint arXiv:2603.18797*, 2026.

- [63] Yi Quan, Jinan Ma, Youxun Jin, Jingru Zhou, Ruen Liu, and Weijian Jiang. Prevalence and independent predictors of unruptured intracranial aneurysms: A systematic review and meta-analysis. *Journal of Clinical Neuroscience*, 140:111542, 2025.
- [64] Nikolaus Rauch and Matthias Harders. Interactive synthesis of 3d geometries of blood vessels. In *Eurographics (Short Papers)*, pages 13–16, 2021.
- [65] Rémi Revellin, François Rousset, David Baud, and Jocelyn Bonjour. Extension of murray’s law using a non-newtonian model of blood flow. *Theoretical Biology and Medical Modelling*, 6(1):7, 2009.
- [66] Andrew J Ringer. *Intracranial aneurysms*. Academic Press, 2018.
- [67] Siriprapa Ritraksa and Khamron Mekchay. 3d structural model and visualization of blood vessels based on l-system. *Trends in Sciences*, 18(24):1407–1407, 2021.
- [68] Hans Christian Rundfeldt, Chang Min Lee, Hanyoung Lee, Keun-Hwa Jung, Hyeyeon Chang, and Hyun Jin Kim. Cerebral perfusion simulation using realistically generated synthetic trees for healthy and stroke patients. *Computer Methods and Programs in Biomedicine*, 244:107956, 2024.
- [69] Sylvia Saalfeld, Philipp Berg, Annika Niemann, Maria Luz, Bernhard Preim, and Oliver Beuing. Semiautomatic neck curve reconstruction for intracranial aneurysm rupture risk assessment based on morphological parameters. *International journal of computer assisted radiology and surgery*, 13(11):1781–1793, 2018.
- [70] Seyedeh Fatemeh Salimi Ashkezari, Felicitas J Detmer, Fernando Mut, Bong Jae Chung, Alexander K Yu, Christopher J Stapleton, Alfred P See, Sepideh Amin-Hanjani, Fady T Charbel, Behnam Rezaei Jahromi, et al. Blebs in intracranial aneurysms: prevalence and general characteristics. *Journal of neurointerventional surgery*, 13(3):226–230, 2021.
- [71] Laura M Sangalli, Piercesare Secchi, Simone Vantini, and Alessandro Veneziani. A case study in exploratory functional data analysis: geometrical features of the internal carotid artery. *Journal of the American statistical association*, 104(485):37–48, 2009.
- [72] Wouter I Schievink. Intracranial aneurysms. *New England Journal of Medicine*, 336(1):28–40, 1997.
- [73] Michael Schlichtkrull, Thomas N Kipf, Peter Bloem, Rianne Van Den Berg, Ivan Titov, and Max Welling. Modeling relational data with graph convolutional networks. In *European semantic web conference*, pages 593–607. Springer, 2018.
- [74] Lisa Schneider, Annika Niemann, Oliver Beuing, Bernhard Preim, and Sylvia Saalfeld. Medmeshcnn-enabling meshcnn for medical surface models. *Computer Methods and Programs in Biomedicine*, 210:106372, 2021.
- [75] Matthias Schneider, Johannes Reichold, Bruno Weber, Gábor Székely, and Sven Hirsch. Tissue metabolism driven arterial tree generation. *Medical image analysis*, 16(7):1397–1414, 2012.
- [76] Zachary A Sexton, Dominic Rüttsche, Jessica E Herrmann, Andrew R Hudson, Soham Sinha, Jianyi Du, Daniel J Shiwerski, Anastasiia Masaltseva, Fredrik Samdal Solberg, Jonathan Pham, et al. Rapid model-guided design of organ-scale synthetic vasculature for biomanufacturing. *Science*, 388(6752):1198–1204, 2025.
- [77] Yiying Sheng, Chengjiaao Liao, Weiran Li, Enyu Yang, Yinling Zhu, Hao Sun, and Hwa Liang Leo. Geometry-aware pointnet for rapid prediction of cerebral aneurysm hemodynamics. *Computer Methods and Programs in Biomedicine*, page 109308, 2026.
- [78] Yawar Siddiqui, Antonio Alliegro, Alexey Artemov, Tatiana Tommasi, Daniele Sirigatti, Vladislav Rosov, Angela Dai, and Matthias Nießner. Meshgpt: Generating triangle meshes with decoder-only transformers. In *Proceedings of the IEEE/CVF conference on computer vision and pattern recognition*, pages 19615–19625, 2024.

- [79] Sook Young Sim. Discrepancy between angiography and operative findings of small side wall aneurysms in atherosclerotic parent arteries. *Journal of Cerebrovascular and Endovascular Neurosurgery*, 19(1):44–47, 2017.
- [80] Ashish Sinha and Ghassan Hamarneh. Trind: Representing anatomical trees by denoising diffusion of implicit neural fields. In *International Conference on Medical Image Computing and Computer-Assisted Intervention*, pages 344–354. Springer, 2024.
- [81] Gaochao Song, Zibo Zhao, Haohan Weng, Jingbo Zeng, Rongfei Jia, and Shenghua Gao. Mesh silksong: Auto-regressive mesh generation as weaving silk. *arXiv preprint arXiv:2507.02477*, 2025.
- [82] Miao Song, Simin Wang, Qian Qian, Yuan Zhou, Yi Luo, and Xijun Gong. Intracranial aneurysm cta images and 3d models dataset with clinical morphological and hemodynamic data. *Scientific data*, 11(1):1213, 2024.
- [83] Tianze Sun, Xiwang He, and Zhonghai Li. Digital twin in healthcare: Recent updates and challenges. *Digital health*, 9:20552076221149651, 2023.
- [84] Gonzalo Daniel Maso Talou, Soroush Safaei, Peter John Hunter, and Pablo Javier Blanco. Adaptive constrained constructive optimisation for complex vascularisation processes. *Scientific Reports*, 11(1):6180, 2021.
- [85] Jiayang Tang, Zhaoshuo Li, Zekun Hao, Xian Liu, Gang Zeng, Ming-Yu Liu, and Qinsheng Zhang. Edgerunner: Auto-regressive auto-encoder for artistic mesh generation. *arXiv preprint arXiv:2409.18114*, 2024.
- [86] Gabriel Taubin. A signal processing approach to fair surface design. In *Proceedings of the 22nd annual conference on Computer graphics and interactive techniques*, pages 351–358, 1995.
- [87] Mihail Ivilinov Todorov, Johannes Christian Paetzold, Oliver Schoppe, Giles Tetteh, Suprosanna Shit, Velizar Efremov, Katalin Todorov-Völgyi, Marco Düring, Martin Dichgans, Marie Piraud, et al. Machine learning analysis of whole mouse brain vasculature. *Nature methods*, 17(4):442–449, 2020.
- [88] Alexander Tong, Kilian Fatras, Nikolay Malkin, Guillaume Huguet, Yanlei Zhang, Jarrid Rector-Brooks, Guy Wolf, and Yoshua Bengio. Improving and generalizing flow-based generative models with minibatch optimal transport. *arXiv preprint arXiv:2302.00482*, 2023.
- [89] Alexandre Vallée. Digital twin for healthcare systems. *Frontiers in Digital Health*, 5:1253050, 2023.
- [90] Boris van Breugel, Tennison Liu, Dino Oglic, and Mihaela van der Schaar. Synthetic data in biomedicine via generative artificial intelligence. *Nature Reviews Bioengineering*, 2(12):991–1004, 2024.
- [91] Ashish Vaswani, Noam Shazeer, Niki Parmar, Jakob Uszkoreit, Llion Jones, Aidan N Gomez, Łukasz Kaiser, and Illia Polosukhin. Attention is all you need. *Advances in neural information processing systems*, 30, 2017.
- [92] MC Villa-Uriol, G Berti, DR Hose, A Marzo, A Chiarini, J Penrose, J Pozo, JG Schmidt, P Singh, R Lycett, et al. @ neurist complex information processing toolchain for the integrated management of cerebral aneurysms. *Interface Focus*, 1(3):308–319, 2011.
- [93] Jörg Vollmer, Robert Mencl, and Heinrich Mueller. Improved laplacian smoothing of noisy surface meshes. In *Computer graphics forum*, volume 18, pages 131–138. Wiley Online Library, 1999.
- [94] Iris Vos, Ynte Ruigrok, Edwin Bennink, Myrthe Buser, Birgitta Velthuis, and Hugo Kuijf. Data of the Circle of Willis Intracranial Artery Classification and Quantification (CROWN) Challenge, 2023. URL <https://doi.org/10.34894/R05G1L>.

- [95] Zhengyi Wang, Jonathan Lorraine, Yikai Wang, Hang Su, Jun Zhu, Sanja Fidler, and Xiaohui Zeng. Llama-mesh: Unifying 3d mesh generation with language models. *arXiv preprint arXiv:2411.09595*, 2024.
- [96] Haohan Weng, Yikai Wang, Tong Zhang, CL Chen, and Jun Zhu. Pivotmesh: Generic 3d mesh generation via pivot vertices guidance. *arXiv preprint arXiv:2405.16890*, 2024.
- [97] Haohan Weng, Zibo Zhao, Biwen Lei, Xianghui Yang, Jian Liu, Zeqiang Lai, Zhuo Chen, Yuhong Liu, Jie Jiang, Chunchao Guo, et al. Scaling mesh generation via compressive tokenization. In *Proceedings of the Computer Vision and Pattern Recognition Conference*, pages 11093–11103, 2025.
- [98] Jianhuang Wu, Qingmao Hu, and Xin Ma. Comparative study of surface modeling methods for vascular structures. *Computerized Medical Imaging and Graphics*, 37(1):4–14, 2013.
- [99] Xiaoyang Wu, Li Jiang, Peng-Shuai Wang, Zhijian Liu, Xihui Liu, Yu Qiao, Wanli Ouyang, Tong He, and Hengshuang Zhao. Point transformer v3: Simpler, faster, stronger. In *Proceedings of the IEEE/CVF Conference on Computer Vision and Pattern Recognition*, 2024.
- [100] Chao Xu, Pei Wu, Bowen Sun, Shancai Xu, Bin Luo, Xinjian Yang, and Huaizhang Shi. Incomplete occlusion and visual symptoms of peri-ophthalmic aneurysm after treatment with a pipeline embolization device: a multi-center cohort study. *Acta Neurochirurgica*, 164(8): 2191–2202, 2022.
- [101] Kaiyuan Yang, Fabio Musio, Yihui Ma, Norman Juchler, Johannes C Paetzold, Rami Al-Maskari, Luciano Höher, Hongwei Bran Li, Ibrahim Ethem Hamamci, Anjany Sekuboyina, et al. Benchmarking the cow with the topcow challenge: Topology-aware anatomical segmentation of the circle of willis for cta and mra. *ArXiv*, pages arXiv–2312, 2025.
- [102] Xi Yang, Ding Xia, Taichi Kin, and Takeo Igarashi. Intra: 3d intracranial aneurysm dataset for deep learning. In *The IEEE Conference on Computer Vision and Pattern Recognition (CVPR)*, 2020.
- [103] An Zeng, Chunbiao Wu, Guisen Lin, Wen Xie, Jin Hong, Meiping Huang, Jian Zhuang, Shanshan Bi, Dan Pan, Najeeb Ullah, et al. Imagecas: A large-scale dataset and benchmark for coronary artery segmentation based on computed tomography angiography images. *Computerized Medical Imaging and Graphics*, 109:102287, 2023.
- [104] Susan Zhang, Stephen Roller, Naman Goyal, Mikel Artetxe, Moya Chen, Shuohui Chen, Christopher Dewan, Mona Diab, Xian Li, Xi Victoria Lin, et al. Opt: Open pre-trained transformer language models. *arXiv preprint arXiv:2205.01068*, 2022.
- [105] Ruowen Zhao, Junliang Ye, Zhengyi Wang, Guangce Liu, Yiwen Chen, Yikai Wang, and Jun Zhu. Deepmesh: Auto-regressive artist-mesh creation with reinforcement learning. In *Proceedings of the IEEE/CVF International Conference on Computer Vision*, pages 10612–10623, 2025.
- [106] Zibo Zhao, Wen Liu, Xin Chen, Xianfang Zeng, Rui Wang, Pei Cheng, Bin Fu, Tao Chen, Gang Yu, and Shenghua Gao. Michelangelo: Conditional 3d shape generation based on shape-image-text aligned latent representation. *Advances in neural information processing systems*, 36:73969–73982, 2023.
- [107] Junsheng Zhou, Jinsheng Wang, Baorui Ma, Yu-Shen Liu, Tiejun Huang, and Xinlong Wang. Uni3d: Exploring unified 3d representation at scale. *arXiv preprint arXiv:2310.06773*, 2023.

## A Technical Appendix: Overview

The appendix provides additional technical details on the individual components of the SynVA toolkit. It includes further information on the morphological parameters (Appx. B), the SynVA-V1 healthy vessel generation model (Appx. C), the GUI for ostium positioning (Appx. D), and the two ostium-conditioned aneurysm generation models SynVA-A1 (Appx. E) and SynVA-A2 (Appx. F). In addition, the procedural pipeline SynVA-P1 (Appx. G) and the generated synthetic dataset (Appx. H) are described in detail, followed by the downstream-task used to validate its usefulness (Appx. I).

## B Morphological Parameters

The characterization of three-dimensional aneurysm morphology is not only valuable as an additional input for deep learning approaches, but also plays a critical role in the assessment of rupture risk. Consequently, several studies have focused on the automatic extraction of morphological parameters from intracranial aneurysms [58, 69]. Building upon these works, we re-implemented the computation of the relevant morphological descriptors within our framework. The resulting parameters are illustrated in Figure 4 and summarized in Table 4.

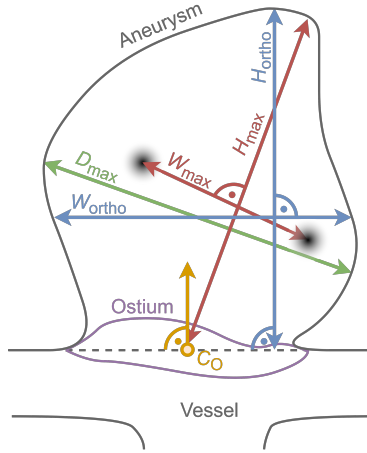


Figure 4: Schematic representation of the aneurysm and the morphological parameters  $H_{\max}$ ,  $W_{\max}$ ,  $H_{\text{ortho}}$ ,  $W_{\text{ortho}}$ , and  $D_{\max}$ . The centroid of the ostium ( $C_O$ ) and its normal vector are also shown. The figure is based on Niemann et al. [58], Saalfeld et al. [69]

The aneurysm surface area  $A_A$  is computed based on the triangular faces of the aneurysm mesh with an open ostium. To estimate the enclosed volume  $V_A$ , the ostium is first sealed using a hole-closing operation, after which the volume is calculated. In cases where a watertight mesh cannot be obtained, the volume of the convex hull  $V_{\text{CH}}$  is used as a fallback approximation. This approximation directly affects derived indices such as  $NSI$  and  $UI$ , with the latter becoming zero in such fallback scenarios.

The ostium area is computed using two complementary approaches. In the first variant,  $A_{O1}$  is defined as the sum of triangular faces formed by pairs of adjacent ostium vertices and the ostium centroid  $C_O$ . In the second variant, all ostium vertices are projected onto the plane defined by the ostium centroid  $C_O$ , and the area  $A_{O2}$  is subsequently calculated in this planar domain.

Geometric extent measures are defined next. The maximum diameter  $D_{\max}$  corresponds to the largest Euclidean distance between any two vertices of the aneurysm mesh. In contrast, the maximum height  $H_{\max}$  is defined as the largest distance between an aneurysm vertex and the ostium centroid  $C_O$ . Based on this principal direction, the maximum width  $W_{\max}$ —measured perpendicular to the vector defined by  $H_{\max}$ —is computed using a ray-casting approach. Specifically, for each vertex, a ray is cast toward the closest point on the  $H_{\max}$  axis, and the corresponding intersection point on the opposite side of the aneurysm surface is determined. The Euclidean distance between the vertex and this intersection point is then evaluated across all vertices, with the maximum value defining  $W_{\max}$ .

Table 4: Morphological parameters used in this work and their definitions [58, 69]. Units are omitted, as the synthetic meshes are not defined in an absolute physical scale. When applied to real-world data, lengths, areas, and volumes correspond to physical units (e.g., mm, mm<sup>2</sup>, mm<sup>3</sup>).

| Feature            | Description   |
|--------------------|---|
| $A_A$              | Aneurysm area excluding the ostium  |
| $V_A$              | Aneurysm volume (closed ostium)   |
| $A_{O1}$           | Ostium area (variant 1, not flattened)  |
| $A_{O2}$           | Ostium area (variant 2, flattened)  |
| $D_{\max}$         | Maximum aneurysm diameter   |
| $H_{\max}$         | Maximum aneurysm height from $C_O$  |
| $W_{\max}$         | Maximum aneurysm width perpendicular to $H_{\max}$  |
| $H_{\text{ortho}}$ | Maximum aneurysm height perpendicular to the ostium plane                                       |
| $W_{\text{ortho}}$ | Maximum aneurysm width perpendicular to $H_{\text{ortho}}$                                      |
| $N_{\max}$         | Maximum ostium diameter   |
| $N_{\text{avg}}$   | Average ostium diameter   |
| $AR_1$             | Aspect ratio: $AR_1 = H_{\text{ortho}}/N_{\max}$  |
| $AR_2$             | Aspect ratio: $AR_2 = H_{\text{ortho}}/N_{\text{avg}}$  |
| $A_{\text{CH}}$    | Area of the convex hull of the aneurysm   |
| $V_{\text{CH}}$    | Volume of the convex hull of the aneurysm   |
| $EI$               | Ellipticity index: $EI = 1 - (18\pi)^{\frac{1}{3}} V_{\text{CH}}^{\frac{2}{3}} / A_{\text{CH}}$ |
| $NSI$              | Non-sphericity index: $NSI = 1 - (18\pi)^{\frac{1}{3}} V_A^{\frac{2}{3}} / A_A$                 |
| $UI$               | Undulation index: $UI = 1 - \frac{V_A}{V_{\text{CH}}}$  |

The orthogonal measures  $H_{\text{ortho}}$  and  $W_{\text{ortho}}$  are computed analogously. The key distinction is that  $H_{\text{ortho}}$  is defined as the maximum distance from aneurysm vertices to the ostium surface, rather than to the centroid.

Finally, ostium-related size measures are derived. The parameter  $N_{\max}$  is computed analogously to  $D_{\max}$ , but restricted to ostium vertices. The average ostium diameter  $N_{\text{avg}}$  is defined as twice the mean distance between all ostium vertices and the centroid  $C_O$ .

All remaining morphological metrics are described in Table 4.

## C SynVA-V1: Vessel Generation

SynVA-V1 is a tree flow-matching-based model for the synthesis of healthy vessel meshes. The approach follows a two-stage design that explicitly separates topology generation from topology-conditioned geometry synthesis. This decomposition enables structured modeling of vascular trees while allowing flexible and precise control over geometric detail. An overview of the architecture is shown in Fig. 5.

### C.1 Data Pre-processing

Our pipeline for converting a raw vessel mesh into a rooted spline tree is adapted from VesselGPT [20]. For each raw vessel mesh, we extract the vessel centerline graph using the *vmtknetworkextraction* script from VMTK [4]. The script traces the centerline by marching along the vessel in steps proportional to the local vessel radius; the proportionality factor (the *advancement ratio*) is initially set to 1.05, and we fall back to the more conservative values 1.02 and 1.01 if the previous run does not return a valid centerline network. The extracted branches are stored as polylines, with one vessel radius assigned to each point. To obtain a consistent resolution along the centerline, each branch is resampled with a default point spacing of 0.02. The spacing is locally reduced in regions where the vessel radius changes strongly and near bifurcations, so that geometrically important areas are represented with higher detail. For every resampled centerline point, we estimate the local tangent from neighboring polyline segments and cut the mesh with the corresponding orthogonal plane. If the cut produces several contour components, only the component closest to the centerline point is kept. Radial outliers are removed before fitting the remaining contour with a closed periodic cubic

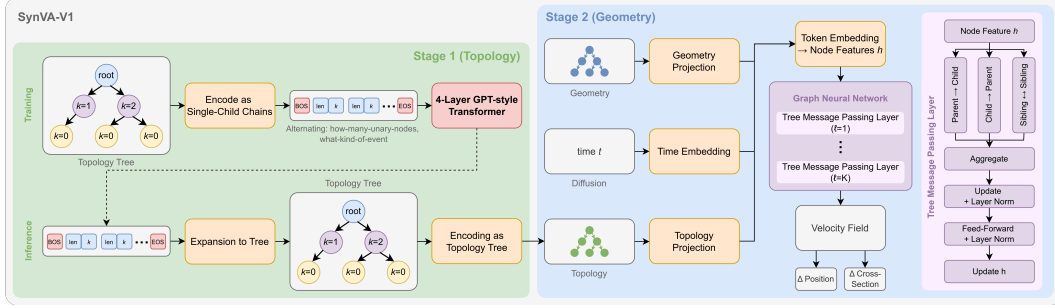


Figure 5: Overview of the SynVA-V1 architecture. **Stage 1 (Topology, green).** The rooted tree is encoded as a sequence of  $(\ell_e, \delta_e)$  pairs alternating chain length and event type, and modeled by a 4-layer GPT-style autoregressive Transformer; at inference, the sampled sequence is expanded back into a topology tree. **Stage 2 (Geometry, blue).** Given the topology, the noisy per-node geometry and the diffusion time  $t$  are projected into per-node token embeddings  $h$  and processed by  $K=10$  Tree Message Passing Layers; a final linear head outputs the per-node velocity, split into  $\Delta$  position and  $\Delta$  cross-section. **Right (pink).** A single Tree Message Passing Layer aggregates parent $\rightarrow$ child, child $\rightarrow$ parent and sibling $\leftrightarrow$ sibling messages, followed by Update + LayerNorm and Feed-Forward + LayerNorm.

B-spline. Each fitted cross-section is then projected onto a fixed periodic basis with 8 control points and 12 knots. As a result, each cross-section is represented by 36 scalar values: 24 control-point coordinates and 12 knot values. The resampled centerline graph is then converted into a rooted tree. The resampled centerline points become nodes, and neighboring points along each polyline are connected by edges. Bifurcation points shared by multiple branches are merged into single graph nodes, and nodes with more than two children are binarized to obtain a binary branching structure. To select a root, we compute all-pairs shortest paths with the Floyd–Warshall algorithm [21], identify the longest graph diameter, and place the root at its midpoint. Starting from this root, a pre-order traversal produces the final ordered tree sequence. Each tree node stores a continuous feature vector  $\mathbf{x}_i = (\mathbf{p}_i, \mathbf{c}_i, \mathbf{s}_i) \in \mathbb{R}^{39}$ , where  $\mathbf{p}_i \in \mathbb{R}^3$  denotes the position of node  $i$ ,  $\mathbf{c}_i \in \mathbb{R}^{24}$  contains the cross-section control points, and  $\mathbf{s}_i \in \mathbb{R}^{12}$  contains the corresponding B-spline knots. In addition, each node is assigned a discrete child-count token  $k_i \in \{0, 1, 2\}$ , which indicates whether the node has zero, one, or two children. This yields a rooted spline tree with a fixed continuous node representation and an explicit discrete topology.

For SynVA-V1<sub>topology</sub>, only the discrete topology of the rooted spline tree is modeled. We therefore discard the continuous node features  $\mathbf{x}_i$  and use only the child-count tokens  $k_i \in \{0, 1, 2\}$ . We traverse the tree in pre-order and compress the resulting child-count sequence by collapsing each chain of consecutive single-child continuation nodes ( $k_i = 1$ ) into a single length value, which is attached to the next leaf or bifurcation. The compressed sequence thus consists only of events — leaves, bifurcations, and the possible single-child root continuation — and each event is represented by a pair  $(\ell_e, \delta_e)$ , where  $\ell_e \in \{0, \dots, L_{\max}\}$  is the length of the preceding  $k_i=1$  chain and  $\delta_e \in \{0, 1, 2\}$  is the event degree. Here,  $\delta_e = 0$  corresponds to a leaf,  $\delta_e = 1$  to a single-child root continuation, and  $\delta_e = 2$  to a bifurcation.

For TreeFlowNet (main backbone of our geometry model), we keep the full continuous feature vector  $\mathbf{x}_i = (\mathbf{p}_i, \mathbf{c}_i, \mathbf{s}_i)$  of every node and pair it with three discrete structure tokens that describe the conditioning topology  $\mathcal{T}$ : the child count  $k_i$  from above, the node depth  $d_i$ , and the child slot  $s_i \in \{1, 2\}$  identifying which sibling position the node occupies under its parent. The position  $\mathbf{p}_i$  is converted from absolute to parent-relative form, so that the model reconstructs the displacement to the parent rather than the global location. Tree edges that are very short relative to the local vessel radius are typically spurious branches introduced by the centerline extraction, and we drop them with a length filter that distinguishes by edge type: an edge into a single-child node (a *continuation edge*) is kept only if its length exceeds the local vessel radius ( $\alpha_{\text{cont}}=1.0$ ), while an edge into a bifurcation is already kept at  $0.30\times$  the local radius ( $\alpha_{\text{bif}}=0.30$ ), so that genuine branching points are preserved even when locally short. The remaining 39 channels of  $\mathbf{x}_i$  are then  $z$ -normalized using the training-set statistics, with the per-channel scale set to the 99.9th percentile and values clipped to  $\pm 3$  to suppress outliers. For the SynVA-V1<sub>aligned</sub> variant only, every cross-section ring is

additionally rotated around the centerline so that its first control point lies at a fixed reference angle; this removes the otherwise arbitrary starting angle of each ring, which would differ from cross-section to cross-section. SynVA-V1<sub>base</sub> and SynVA-V1<sub>depth</sub> use the rings as extracted, without this rotational alignment. During training, the conditioning topology  $\mathcal{T}$  is the ground-truth topology of the same tree; at inference,  $\mathcal{T}$  is either taken from the test-set ground truth (for the evaluation reported here) or sampled from SynVA-V1<sub>topology</sub>.

## C.2 Architecture

SynVA-V1<sub>topology</sub> (Fig. 5, Stage 1) is a small GPT-2-style autoregressive Transformer decoder  $p_\phi(\mathcal{T})$  [91]. The vocabulary has  $|\mathcal{V}| = 70$  tokens in three groups: 64 chain-length tokens  $\ell_e \in \{0, \dots, L_{\max}=63\}$  that count consecutive single-child continuation nodes, 3 event-degree tokens  $\delta_e \in \{0, 1, 2\}$  for the three event types (leaf, single-child root continuation, bifurcation), and the 3 special tokens BOS, EOS and PAD. The decoder has 4 Transformer layers, 128-dim token embeddings, 4 attention heads, and dropout 0.15 on the residual, attention and embedding paths.

TreeFlowNet (Fig. 5, Stage 2) is a topology-conditioned velocity field  $v_\theta(\mathbf{x}_t, t \mid \mathcal{T}) \in \mathbb{R}^{N \times 39}$ , implemented as a typed message-passing GNN [25, 73] with sparse global self-attention [91] interleaved every  $g=3$  layers. Each node is embedded into a token feature  $h_i^{(0)} \in \mathbb{R}^d$  ( $d=256$ ) from three input streams. The discrete structure tokens  $(k_i, d_i, s_i)$  are passed through three separate learned embedding tables, the results are concatenated and projected by a small GELU MLP into a structural embedding; the noisy geometry  $\mathbf{x}_{i,t}$  at diffusion time  $t$  is mapped to  $\mathbb{R}^d$  by a linear projection; and the diffusion time  $t$  itself is encoded by a sinusoidal embedding. The structural and geometry features are concatenated and linearly projected back to  $\mathbb{R}^d$ , the time embedding is then added, and the sum is passed through LayerNorm.  $K=10$  TreeMessagePassingLayer blocks (Fig. 5, right) then update  $h_i$  as follows. Every edge of the tree falls into one of three types read from the parent index  $\pi$  — parent→child, child→parent or sibling↔sibling — and each type is associated with its own edge-type-specific message MLP. For every edge, the source and destination node features are concatenated and passed through the corresponding MLP to produce a per-edge message. At each node, all incoming messages are summed, concatenated with the current node feature, passed through an update MLP, added back as a residual, and LayerNormed. A feed-forward + LayerNorm residual closes the block, and every  $g=3$  layers a global multi-head self-attention block (8 heads) re-mixes long-range tree context. After the last block, a linear head projects  $h_i$  back to  $\mathbb{R}^{39}$ , giving the per-node velocity  $v_\theta(\mathbf{x}_t, t \mid \mathcal{T})_i$ .

To generate new synthetic vessels, SynVA-V1<sub>topology</sub> first samples a topology  $\mathcal{T}$  via nucleus decoding (temperature 1.0, top- $p=0.95$ ) under the grammar mask described below, so the decoded sequence is guaranteed to expand into a valid binary tree of  $N$  nodes. TreeFlowNet then samples the conditioning geometry by integrating the ODE  $\dot{\mathbf{x}}_t = v_\theta(\mathbf{x}_t, t \mid \mathcal{T})$  from  $\mathbf{x}_0 = \mathbf{z} \sim \mathcal{N}(0, I) \in \mathbb{R}^{N \times 39}$  to  $\mathbf{x}_1$  with 100 Euler steps under the topology  $\mathcal{T}$ . The clean per-node vectors  $\mathbf{x}_i^{(1)} = (\mathbf{p}_i, \mathbf{c}_i, \mathbf{s}_i)$  are then de-normalized with the training-set  $\mathbf{z}$  statistics, the parent-relative positions  $\mathbf{p}_i$  are accumulated into absolute coordinates by a single traversal from the root, and each cross-section ring is re-constructed from its 8 control points  $\mathbf{c}_i$  and 12 B-spline knots  $\mathbf{s}_i$ . The result is a clean rooted spline tree, ready for the mesh-reconstruction pipeline below.

Predicted spline trees are converted to watertight surfaces in five deterministic stages: arc-length spline-station interpolation ( $\Delta s=0.005$ ) of 64-point cross-section rings; per-segment screened-Poisson reconstruction [36] at octree depth  $D=8$  with end caps suppressed at bifurcations; Boolean union of the per-segment tubes; localized Laplacian and Taubin [86] smoothing in  $3 \times$  local-radius balls around bifurcation centers; and a global re-Poisson pass at depth  $D'=9$ .

## C.3 Training Details

We adopt the same train/test splits as every other model in this work (see Section 3.5), and apply for each training sample 10 different random rotations. The topology model and the geometry model of SynVA-V1 are then trained independently on the prepared trees. SynVA-V1<sub>topology</sub> is optimized for 160 epochs with AdamW (lr  $3 \times 10^{-4}$ , weight decay 0.02, cosine schedule, batch size 32, dropout 0.15). Training minimizes a next-token cross-entropy loss on the topology sequence of event pairs  $(\ell_e, \delta_e)$ . At inference, tokens are sampled autoregressively with nucleus (top- $p$ ) decoding under a hard grammar mask: before every step, the logits of all tokens that would violate the rooted-

tree grammar are set to  $-\infty$ , so that they can never be drawn. Masked cases include a length token where a degree token is expected (and vice versa, since events strictly alternate  $\ell_e, \delta_e$ ), a degree-1 event after the first event (the single-child root continuation may only occur once, at the start), and an EOS while child slots are still open. Every sampled sequence therefore decodes into a valid rooted binary tree

TreeFlowNet is optimized for 400 epochs with AdamW (lr  $2 \times 10^{-4}$ , weight decay 0.01, 500-step linear warm-up, batch size 64, seed 42) under the optimal-transport conditional flow-matching loss [48, 88]

$$\mathcal{L}_{\text{FM}} = \mathbb{E}_{t, \mathbf{x}_0, \mathbf{z}} \left\| v_\theta((1-t)\mathbf{z} + t\mathbf{x}_0, t \mid \mathcal{T}) - (\mathbf{x}_0 - \mathbf{z}) \right\|_{2,m}^2, \quad (1)$$

where  $\mathbf{x}_0$  is the ground-truth per-node geometry of a training tree under topology  $\mathcal{T}$ ,  $\mathbf{z} \sim \mathcal{N}(0, I)$ , and  $\|\cdot\|_{2,m}$  is a masked block-weighted norm over the position, cross-section and knot channels of  $\mathbf{x}_i = (\mathbf{p}_i, \mathbf{c}_i, \mathbf{s}_i)$  with weights  $(\lambda_p, \lambda_c, \lambda_s) = (1, 1, 0.5)$ , complemented by auxiliary regularizers — knot monotonicity (0.5), cross-section planarity (1.0) and radius consistency (3.0) — that act on the same blocks.

#### C.4 Experimental Setting

The main paper reports three TreeFlowNet variants. They all share the same backbone, optimizer and base flow-matching loss; the only differences are how the diffusion time  $t$  is sampled during training, how individual nodes are weighted in the loss, and whether the cross-section rings of the training data are pre-aligned.

SynVA-V1<sub>base</sub> is the simplest version. During training the diffusion time  $t$  is drawn uniformly from  $[0, 1]$ , every node contributes equally to the loss, and the cross-section rings are used in their original orientation. We use this configuration as the reference against which the other two are compared.

SynVA-V1<sub>depth</sub> adds a node-dependent rescaling of the diffusion time. Instead of feeding the same  $t$  into the time embedding of every node, each node  $i$  at depth  $d_i$  sees  $\hat{t}_i = t \cdot \alpha^{d_i}$  with  $\alpha = 0.5$ , so deeper nodes effectively train at a lower noise level for any given global  $t$ . In practice this lets the smaller, deeper branches converge faster, while the overall flow-matching schedule from  $t=0$  to  $t=1$  is left unchanged.

SynVA-V1<sub>aligned</sub> adds three further changes on top of SynVA-V1<sub>depth</sub>. First, the diffusion time is drawn from a logit-normal  $t = \sigma(\mu + s\varepsilon)$  with  $\varepsilon \sim \mathcal{N}(0, 1)$ ,  $\mu=0$ ,  $s=1$  [18] instead of uniformly, which concentrates training samples in the mid-noise regime where the velocity field is hardest to fit. Second, the position channel of the loss is multiplied by a Gaussian focal weight  $w_i^{\text{focal}} = 1 + \lambda_f \exp(-\|\mathbf{p}_i\|^2 / 2\sigma_f^2)$  with  $\lambda_f=4$  and  $\sigma_f=0.05$ , which up-weights short continuation segments whose parent-relative position is close to zero. Third, training uses the cross-section-aligned dataset variant in which all cross-section rings start at a consistent angular offset; this removes the rotational ambiguity of the 8 ring control points  $\mathbf{c}_i$ .

Distribution-level metrics (MMD [26], COV [1], 1-NNA [49]) operate on a 13-dimensional per-tree descriptor of geometry-only summary statistics ( $z$ -normalized on the GT set; topology-derived features are excluded since topology is conditioned on the GT). `cos_radius` is the cosine similarity between the global branch-radius histograms of all GT and all generated trees [19]. Topology metrics ( $\text{KL}_{\text{degree}}$  and a Laplacian-spectrum distance *Spec*. [8]) are computed on the same trees with their published definitions.

#### C.5 Additional Results

Table 5 lists all TreeFlowNet variants we evaluated on the test set. The three configurations reported in the main paper (SynVA-V1<sub>base</sub>, SynVA-V1<sub>depth</sub>, SynVA-V1<sub>aligned</sub>) are highlighted in bold; the remaining rows toggle individual design knobs on top of these. The second block activates the full physiological auxiliary loss family (Murray’s law [54], target bifurcation angle  $\theta^*$ , sibling cosine, symmetry, depth-radius shrinkage) and was excluded from the main paper because it distorts local branching geometry, as visible from the large `BifAngle` deviation from the GT mean of  $75.9^\circ$ . The third block (SynVA-V1<sub>phys-Tx</sub>) replaces the TreeFlowNet GNN backbone with a flat self-attention Transformer while keeping the same physiological loss family as SynVA-V1<sub>phys</sub>, isolating the contribution of typed message passing under matched supervision.

On top of SynVA-V1<sub>base</sub>, SynVA-V1<sub>depth</sub>, and SynVA-V1<sub>aligned</sub> (defined above), the remaining variants are as follows. *Logit-time* replaces the uniform diffusion-time sampler with a logit-normal  $t = \sigma(\mu + s\varepsilon)$  on top of SynVA-V1<sub>depth</sub>, without focal weight or ring alignment. *Focal-pos*  $\lambda=2/4$  adds a Gaussian focal weight on the position channel of the loss with strength  $\lambda$  on top of SynVA-V1<sub>depth</sub>, and *focal-pos + cp-bif* additionally up-weights the cross-section channels at bifurcation nodes by  $3\times$  (with  $\lambda=2$ ). *Aligned-45°* is the same recipe as SynVA-V1<sub>aligned</sub> but with a tighter 45° ring-tilt threshold so that more rings are re-rotated, and *anti-curl-back* adds a sibling-separation hinge loss preventing the two child branches from initially curling back together right after a bifurcation. The physiological block activates the full physiological auxiliary loss family on top of SynVA-V1<sub>depth</sub>: *physio-wide* uses the upstream target  $\theta^*=120^\circ$ ; *physio-wide, no-warp* additionally drops the depth-warp; SynVA-V1<sub>phys</sub> uses the corrected angle target  $\theta^*=50^\circ$  (closer to the GT median of  $\approx 47^\circ$ ); and SynVA-V1<sub>combined</sub> couples SynVA-V1<sub>phys</sub> with focal-pos  $\lambda=4$  and anti-curl-back, combining the strongest knobs from both blocks.

Table 5: Full ablation of all 14 TreeFlowNet-family variants on the test set ( $n=60$ ). Boldfaced rows are the three configurations reported in the main paper. Per-column best is bold within each block; GT row is the reference.

| Variant   | MMD↓         | 1-NNA→.5     | BifAngle→75.9° | Chamfer (mesh)↓ |
|---|--------------|--------------|----------------|-----------------|
| <i>TreeFlowNet variants (typed message-passing GNN backbone)</i>              |              |              |                |                 |
| SynVA-V1 <sub>base</sub> (plain base)   | 0.042        | 0.725        | 83.5°          | 0.325           |
| SynVA-V1 <sub>depth</sub> (depth-warp)  | <b>0.040</b> | 0.717        | 83.5°          | 0.324           |
| logit-time  | 0.080        | <b>0.617</b> | 83.8°          | 0.330           |
| focal-pos $\lambda=2$   | 0.069        | <b>0.617</b> | 86.3°          | 0.330           |
| focal-pos $\lambda=4$   | 0.070        | 0.667        | 86.8°          | 0.331           |
| focal-pos + cp-bif  | 0.077        | 0.692        | 82.6°          | 0.337           |
| SynVA-V1 <sub>aligned</sub> (aligned-60°)                                     | 0.077        | 0.700        | <b>80.8°</b>   | 0.331           |
| aligned-45°   | 0.085        | 0.717        | 83.9°          | 0.333           |
| anti-curl-back  | 0.081        | 0.658        | 88.2°          | 0.335           |
| <i>TreeFlowNet variants with the full physiological auxiliary loss family</i> |              |              |                |                 |
| physio-wide ( $\theta^*=120^\circ$ )  | 0.098        | 0.750        | 122.4°         | 0.328           |
| physio-wide, no-warp ( $\theta^*=120^\circ$ )                                 | 0.108        | 0.742        | 122.1°         | 0.327           |
| SynVA-V1 <sub>phys</sub> ( $\theta^*=50^\circ$ )                              | 0.084        | 0.775        | 105.2°         | 0.324           |
| SynVA-V1 <sub>combined</sub> (combined)                                       | 0.071        | 0.717        | 103.9°         | 0.316           |
| <i>Transformer baseline (flat self-attention, no GNN message passing)</i>     |              |              |                |                 |
| SynVA-V1 <sub>phys-Tx</sub> ( $\theta^*=50^\circ$ )                           | 0.129        | 0.908        | 98.6°          | <b>0.304</b>    |
| GT  | 0            | 0.500        | 75.9°          | 0               |

SynVA-V1<sub>base</sub>, SynVA-V1<sub>depth</sub> and SynVA-V1<sub>aligned</sub> are the only variants that pull the mean bifurcation angle close to the GT mean of 75.9° ( $83.5^\circ \rightarrow 83.5^\circ \rightarrow 80.8^\circ$ ) at no measurable cost on MMD or 1-NNA, whereas the rest of the non-physio block (logit-time, focal-pos, cp-bif, aligned-45°, anti-curl-back) matches SynVA-V1<sub>base</sub> on the distribution metrics but stays further from the GT angle. The physiological loss family makes the picture worse, not better: SynVA-V1<sub>phys</sub> with the corrected target  $\theta^*=50^\circ$  still settles around 104° ( $\sim 30^\circ$  above the GT), and the upstream default  $\theta^*=120^\circ$  pushes the angle out to  $\sim 122^\circ$  while MMD (0.098) and 1-NNA (0.750) deteriorate along the way. The Transformer baseline SynVA-V1<sub>phys-Tx</sub> wins on mesh Chamfer (0.304) but is worst on 1-NNA (0.908, far from the indistinguishability target of 0.5): its Chamfer gain comes from aggregate volume overlap rather than per-tree similarity, and the 1-NNA gap shows that for local plausibility the typed message passing of TreeFlowNet matters more than the larger receptive field of a flat self-attention backbone. We therefore report SynVA-V1<sub>base</sub>, SynVA-V1<sub>depth</sub> and SynVA-V1<sub>aligned</sub> in the main paper — they hit the best balance between anatomical plausibility and distribution similarity, while every remaining variant fails on either anatomy (physio family) or distribution (Transformer baseline).

### C.5.1 Foundation-model t-SNE: GT vs. Reconstructed Meshes

To assess whether the reconstructed meshes of the three reported configurations are visually distinguishable from the GT meshes, we embed each mesh with the UNI3D-G foundation model [107]: every mesh is sampled to 10 000 surface points, normalized to the unit sphere, and mapped to a 1024-dim feature vector. The features of all four sources (GT and the three reported configurations)

are projected jointly to two dimensions with t-SNE (perplexity 30, PCA initialization, 1500 iterations, seed 42).

Fig. 6 shows the resulting embedding between the original high-resolution GT meshes and our spline-Poisson reconstructions of SynVA-V1<sub>base</sub>, SynVA-V1<sub>depth</sub> and SynVA-V1<sub>aligned</sub>. The reconstructed meshes lie well within the GT cloud, and the four sources interleave throughout the embedding without forming any contiguous single-source cluster — meaning that our predictions are essentially indistinguishable from the GT in the UNI3D feature space.

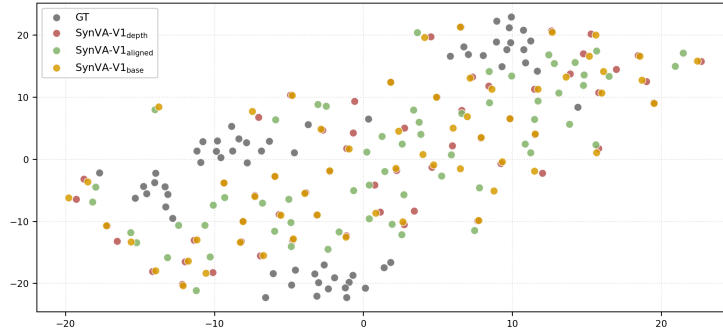


Figure 6: t-SNE embeddings of ground-truth and topology-conditioned synthetic healthy vessels from the three SynVA-V1 geometry models.

## D Graphical User Interface for Ostium Selection

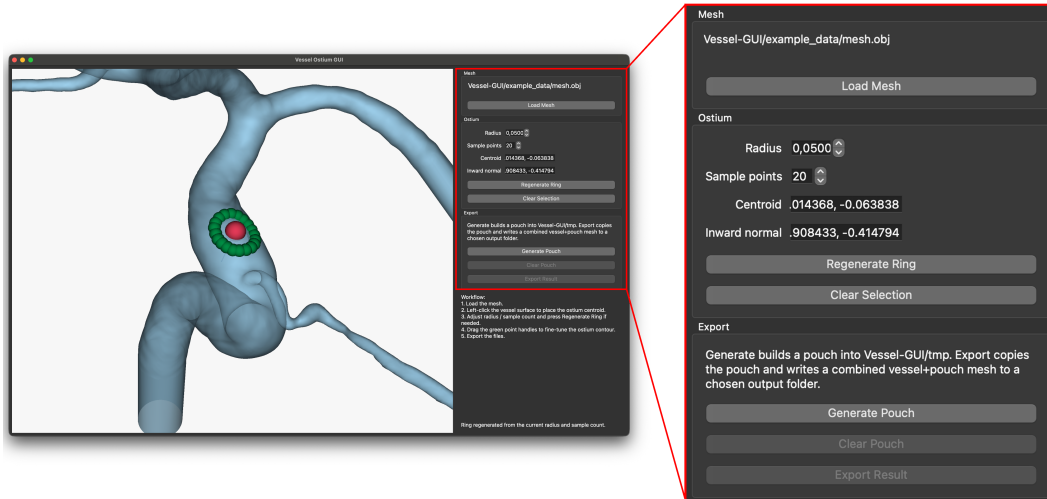


Figure 7: GUI for ostium placement and contour editing. The tool supports interactive ring adjustment, vessel cutting, and exports the ostium centroid and inward normal for downstream processing.

The graphical user interface (GUI) shown in Figure 7 enables the user to select a vertex on the vessel surface to define the ostium centroid. A surface normal is estimated from the local geometry, and an editable circular contour with a user-defined radius is generated at this location. The vessel surface is subsequently clipped using `vtkSelectPolyData` and `vtkClipPolyData`, resulting in an opening that defines the attachment site of the aneurysm.

The resulting ostium and associated normal vector serve as inputs for generating an aneurysm pouch using the models introduced in this work. To ensure watertight connectivity between the vessel and the synthesized aneurysm, boundary loops are extracted from both geometries and stitched together. The resulting junction is further refined via an  $N$ -hop neighborhood averaging scheme to ensure smooth geometric transitions.

## E SynVA-A1

The SynVA-A1 model is based on the concept introduced in AneuG [15], and extends it to conditionally generate aneurysm geometries on pre-existing healthy vascular structures. Conditioning is performed on the ostium as well as on local vessel geometry and morphological parameters, enabling the synthesis of realistic aneurysmal deformations directly on anatomically plausible vessel segments. This design is motivated by the observation that, in nature, aneurysms do not arise in isolation but develop from previously healthy vessels. Consequently, modeling aneurysm formation as a conditional transformation of healthy vasculature not only aligns with the underlying biological process but also enables the systematic conversion of arbitrary healthy vessel geometries into pathological counterparts.

### E.1 Data Pre-processing

SynVA-A1 is trained on a real-world dataset from which a canonical mesh is first constructed as the basis for graph harmonic deformation (GHD) fitting. For this purpose, the aneurysm submeshes are used. Prior to fitting, all target aneurysm sacs are first brought into a shared coordinate system through alignment of their respective ostia. Within this shared space, a canonical aneurysm template is constructed from the entire training distribution by applying a ray-casting procedure in which rays are emitted from a common origin and intersect all aligned aneurysm geometries. For each ray direction, the median intersection distance across all aligned training samples is computed, and this statistic defines the vertex position of the canonical mesh along that ray. In this way, the resulting canonical template constitutes a robust statistical average of the dataset geometry under consistent ostium alignment. Subsequently, each target aneurysm is rigidly aligned to this canonical mesh. First, a translation is applied to map the target ostium center to the canonical ostium center. Second, a rotation is performed to align the ostium normal vectors, ensuring consistent orientation across all samples. The resulting transformation matrix  $\mathbf{H}$  is stored for post-processing steps. After this alignment, both canonical and target meshes are normalized.

For SynVA-A1 training, the GHD fitting checkpoint provides the target representation. The target vector consists of the fitted GHD coefficients ( $K = 144$ , three coordinate channels) and the fitted scale. The fitted rotation and translation are not predicted by SynVA-A1; they are used only to define the local GHD coordinate frame and to decode meshes for the training losses. Thus, the encoder does not receive a raw mesh, but the normalized GHD target from the fitting step.

The condition input is extracted from the same case and is centered around the ostium. SynVA-A1 therefore does not use the complete vessel tree as input, but only the local vessel geometry that is relevant for aneurysm attachment. To make this vessel patch consistent with the fitted GHD representation, the candidate vessel points are first mapped into the same local coordinate frame as the fitted aneurysm. Distances are then measured from the ostium-ring centroid, and a neighborhood around the ostium is retained. The neighborhood radius is chosen from the ostium size and the local distance distribution, so that it covers the neck region and nearby parent-vessel surface without including the entire vessel. From this local patch, 256 points are selected by farthest-point sampling. If the local selection contains too few points, the full candidate surface is used as a fallback. The remaining conditioning inputs are the ordered ostium ring, compact ostium parameters consisting of center, normal, radius, and eccentricity, dense attachment samples from the segmented ostium region, and the morphology descriptor vector. The morphology condition is defined by the independent scalar features  $A_A$ ,  $V_A$ ,  $A_{CH}$ ,  $V_{CH}$ ,  $D_{\max}$ ,  $H_{\max}$ ,  $W_{\max}$ ,  $H_{\text{ortho}}$ , and  $W_{\text{ortho}}$ . GHD targets and continuous conditioning variables are normalized with training-set statistics.

### E.2 Architecture

Analogous to AneuG [15], SynVA-A1 consists of two coupled components. First, each training aneurysm is represented via a GHD fit of the aneurysm sac and neck region in a shared canonical eigenspace. Second, SynVA-A1 learns a conditional generative model over the resulting GHD parameters, conditioned on local vessel geometry, ostium information, and global morphological descriptors.

### E.2.1 GHD Fitting

Our fitting procedure builds upon the GHD representation introduced in AneuG [15], but adapts it from full aneurysm–vessel segments, which include the parent artery and multiple openings, to a localized representation focused on the aneurysm sac. In the present setting, the fitting target is defined by the aneurysm sac in combination with a single ostium, which serves as the sole anatomical interface to the parent vessel.

We retain the core GHD representation from AneuG. Each case is fitted by deforming the canonical sac in a shared graph-harmonic basis and by optimizing a global similarity transform. The target of the fit is therefore not a raw mesh with arbitrary topology, but a compact set of GHD coefficients in the common canonical eigenspace. In our implementation this basis contains  $K = 144$  graph-harmonic modes.

The general shape terms are also inherited from the original AneuG fitting objective. We use surface Chamfer distance and surface-normal matching to align the deformed canonical sac with the target sac. We further keep the standard mesh regularizers used in AneuG: Laplacian smoothing, edge-length regularization, normal-consistency regularization, and local rigidity. These terms control the overall sac shape and discourage noisy or folded deformations.

The main methodological change is the treatment of the ostium. Original AneuG supervises several vessel openings and, in its full-vessel setting, can use differentiable occupancy and differentiable centreline losses to constrain the parent-vessel segment. Since SynVA-A1 does not fit the parent vessel, these full vessel losses are disabled in our sac-and-neck fitting mode. Instead, we replace the multi-opening objective by a single-ostium objective. The ostium is represented by an ordered boundary ring and by a reconstructed opening patch from the ostium checkpoint. This allows us to supervise the neck directly: the opening position is matched to the target, the opening normal is aligned using a robust ring-based normal estimate, and an area term prevents collapse of the neck opening. Additional overlap, boundary-smoothness, and relative-volume terms stabilize the vessel–aneurysm interface and the global sac size.

### E.2.2 Conditional Aneurysm Generator

SynVA-A1 models a conditional prior over the fitted GHD parameters of the aneurysm sac and neck region. The generator therefore does not predict mesh vertices directly, but the GHD representation produced by the fitting step. For each case, the target vector contains the  $144 \times 3$  GHD coefficients and the fitted scale. Compared with the AneuGs conditional GHD-VAE backbone, SynVA-A1 changes mainly what the model is conditioned on and how the decoded samples are supervised: it adds local vessel–ostium conditioning, morphology conditioning, geometry-aware ostium supervision, and prior-path calibration for direct samples from the VAE prior.

The condition is built from the local anatomy around the prescribed ostium. The local vessel patch, represented by 256 points, is encoded with a PointNet-style MLP branch followed by max pooling. Low dimensional ostium parameters, consisting of center, normal, radius, and eccentricity, are encoded with a small MLP. The ordered ostium ring is resampled to 20 points, flattened, and encoded with a separate MLP so that the network receives the neck boundary as an explicit geometric signal. These branch embeddings are fused into a 96-dimensional vessel–ostium feature. The selected morphology descriptor vector is appended to this feature, and the resulting condition vector is projected to a 64-dimensional condition embedding. Dense samples from the segmented ostium attachment region are prepared for the same case, but in the final model they are used for interface supervision rather than as an additional condition branch.

The generative backbone is a conditional GHD-VAE. During training, the encoder receives the normalized fitted GHD target and maps it to a Gaussian latent distribution. A latent code is sampled with the standard reparameterization trick and passed to the decoder together with the condition embedding. The decoder then predicts the normalized GHD coefficients and scale. Both encoder and decoder use a linear input projection and one residual MLP block; the hidden dimension is 256 and the latent dimension is 108. At inference time, the fitted target is absent. A latent code is sampled from the standard normal prior and decoded under the same vessel, ostium, and morphology condition.

The additional supervision is tied to this inference setting. The decoded GHD parameters are converted back to a mesh during training, which allows losses at the vessel–aneurysm interface to

constrain the generated neck geometry. Moreover, prior-path calibration explicitly decodes samples from  $z \sim \mathcal{N}(\mathbf{0}, \mathbf{I})$  during training and matches them to case-level and batch-level target statistics. Thus, the model is trained not only to reconstruct fitted targets through the posterior path, but also to produce plausible conditional samples through the same prior path used at test time.

### E.3 Training Details

#### E.3.1 GHD Fitting

The GHD fits are optimized independently for each prepared aneurysm case. We use the precomputed canonical basis with  $K = 144$  and a single ostium. The optimization uses AdamW with learning rate  $2.5 \cdot 10^{-3}$  for 4000 epochs and a step scheduler with step size 1800 and decay factor 0.8. The opening terms are warmed up during the first 500 epochs, and gradients are clipped to improve stability. The active loss weights are listed in Table 6.

Table 6: Loss weights used for the SynVA-A1 GHD fitting.

| Term               | Weight | Term             | Weight |
|--------------------|--------|------------------|--------|
| Surface Chamfer    | 1.50   | Surface normals  | 0.80   |
| Occupancy          | 1.25   | Diff. centreline | 1.00   |
| Laplacian          | 0.12   | Edge length      | 0.12   |
| Normal consistency | 0.12   | Local rigidity   | 12.00  |
| Ordered rim        | 8.00   | Opening surface  | 2.00   |
| Opening normal     | 0.01   | Opening plane    | 20.00  |
| Rim curvature      | 0.60   | Thickness        | 0.05   |

#### E.3.2 SynVA-A1 Training

We use the same stratified and balanced split as the other models in this work: 530 training cases, 132 validation cases, and 100 held-out test cases. The CVAE is trained for 4000 epochs with batch size 96 using AdamW with learning rate  $10^{-4}$  and weight decay  $10^{-4}$ . The latent dimension is 108, the hidden dimension is 256, the condition embedding dimension is 64, and the vessel-condition embedding dimension is 96. The VAE and the vessel-ostium condition network are optimized jointly, without condition dropout in the selected run. We use a KL warm-up of 1000 epochs, free bits of 0.02, gradient clipping with maximum norm 1.0, validation every 50 epochs, and select the checkpoint with the lowest validation total loss. The selected SynVA-A1 checkpoint is from epoch 2550.

The CVAE is trained with three complementary loss groups. First, the posterior path reconstructs the fitted GHD target. During this step, the encoder sees the normalized GHD coefficients and scale of a training aneurysm, samples a latent code with the reparameterization trick, and the decoder reconstructs the same GHD vector under the case-specific condition. This reconstruction is supervised in coefficient space, in the scale value, and after GHD decoding in vertex space. The KL term is warmed up during training and uses free bits to avoid an overly weak latent representation.

Second, we add geometry-aware supervision around the ostium. For this loss group, the reconstructed GHD vector is decoded to a mesh, transformed to the case frame, and aligned to the target ostium ring in the same way as in the later placement step. We then evaluate four local interface losses. The attachment loss measures the nearest-surface distance from dense samples of the segmented ostium attachment region to the generated aneurysm and therefore encourages the generated neck to cover the prescribed attachment area. The sac-center loss compares the center of the generated aneurysm sac, excluding the opening vertices, with the center of the fitted target sac and stabilizes the global placement of the aneurysm relative to the neck. The side loss uses the ostium normal and penalizes generated sacs whose center lies on the wrong side of the ostium plane, which prevents growth through the vessel wall. The opening-center loss compares the mean position of the generated opening ring with the target ostium-ring center. In the selected model, these terms are combined as  $\mathcal{L}_{\text{geo}} = 5.0 \mathcal{L}_{\text{attach}} + 10.0 \mathcal{L}_{\text{center}} + 2.0 \mathcal{L}_{\text{side}} + 10.0 \mathcal{L}_{\text{open}}$ . Together, these losses ensure that a good reconstruction is not only close in GHD space, but also compatible with the prescribed vessel-aneurysm interface.

Third, SynVA-A1 explicitly trains the prior sampling path. This is important because inference does not use the encoder; it samples  $z_{\text{prior}} \sim \mathcal{N}(\mathbf{0}, \mathbf{I})$  and decodes this latent vector under the given condition. We therefore perform the same operation during training in each mini-batch. The resulting

Table 7: CVAE loss weights used for SynVA-A1.

| Term        | Weight | Term               | Weight     |
|-------------|--------|--------------------|------------|
| Coeff. MSE  | 1.0    | Attachment samples | 5.0        |
| Scale Huber | 1.0    | Sac center         | 10.0       |
| Vertex MSE  | 250.0  | Side               | 2.0        |
| KL          | 0.01   | Opening center     | 10.0       |
| Prior Huber | 0.25   | Prior mean/std     | 0.25 / 8.0 |

prior-decoded GHD vector is encouraged to stay close to the paired target, while its batch mean and batch standard deviation are matched to those of the fitted targets. The mean term keeps the samples centered on the training distribution, and the standard-deviation term discourages collapse to an average aneurysm. Overall, the objective contains reconstruction, geometry, and prior-calibration terms, with the weights listed in Table 7.

Evaluation uses paired surface Chamfer distance with 10,000 sampled surface points, mean absolute errors of morphology descriptors, and distribution-level metrics in standardized morphology space: paired  $z$ -L2, generated-to-GT nearest-neighbor distance, GT-to-generated nearest-neighbor distance, coverage, MMD, and Frechet distance.

#### E.4 Experimental Setting

All ablations are trained and evaluated with the same splits and the same 100-case test set. We compare a sequence of variants that progressively add the proposed conditioning and training components. **AneuG-Base** is the AneuG-style conditional GHD-VAE baseline trained on the fitted aneurysm sac and neck GHD parameters. It does not use the proposed local vessel–ostium condition, morphology condition, or prior-path calibration. **AneuG-Cond** adds the local vessel–ostium condition, including the local vessel point set, low-dimensional ostium parameters, and ordered ostium ring. **AneuG-Cond-Morph** extends this variant with the selected morphology descriptor vector. **AneuG-Cond-Prior** instead adds prior-path calibration to AneuG-Cond but omits the morphology condition, which isolates the effect of calibrating direct samples from the VAE prior.

**SynVA-A1** is the selected model and combines local vessel–ostium conditioning, morphology conditioning, geometry-aware ostium supervision, and prior-path calibration. **SynVA-A1-Ostium** uses the same architecture as SynVA-A1, but increases the ostium/interface supervision weights to test whether stronger local neck emphasis improves the generated attachment geometry. Evaluation uses paired surface Chamfer distance with 10k sampled surface points, mean absolute errors of morphology descriptors, and distribution-level metrics in standardized morphology space. Lower values are better for all reported metrics except coverage.

#### E.5 Additional Results

Table 8: Paired aneurysm reconstruction results on the 100 held-out test cases. Values are mean absolute differences with standard deviation, except for Chamfer distance, which is computed from 10k sampled surface points. Lower is better; the best mean value in each row is highlighted.

| Mean Absolute Difference | AneuG-Base      | AneuG-Cond      | AneuG-Cond-Morph       | AneuG-Cond-Prior       | SynVA-A1               | SynVA-A1-Ostium        |
|--------------------------|-----------------|-----------------|------------------------|------------------------|------------------------|------------------------|
| $A_A$                    | 0.2104 ± 0.3245 | 0.1974 ± 0.2960 | 0.1711 ± 0.2807        | 0.1638 ± 0.2661        | 0.1560 ± 0.2599        | <b>0.1555 ± 0.2630</b> |
| $A_{CH}$                 | 0.2123 ± 0.3322 | 0.1962 ± 0.2984 | 0.1744 ± 0.2871        | 0.1625 ± 0.2684        | <b>0.1539 ± 0.2631</b> | 0.1543 ± 0.2682        |
| $D_{max}$                | 0.1133 ± 0.1122 | 0.1068 ± 0.1109 | 0.1079 ± 0.1120        | <b>0.0842 ± 0.0992</b> | 0.0842 ± 0.0992        | 0.0881 ± 0.1008        |
| $H_{max}$                | 0.1199 ± 0.1160 | 0.1087 ± 0.1068 | 0.1037 ± 0.1053        | 0.0814 ± 0.0914        | <b>0.0796 ± 0.0905</b> | 0.0826 ± 0.0924        |
| $H_{ortho}$              | 0.1106 ± 0.1101 | 0.0998 ± 0.1009 | 0.0929 ± 0.0955        | 0.0746 ± 0.0834        | <b>0.0715 ± 0.0821</b> | 0.0743 ± 0.0844        |
| $V_A$                    | 0.0314 ± 0.0630 | 0.0322 ± 0.0623 | 0.0273 ± 0.0595        | 0.0225 ± 0.0462        | 0.0214 ± 0.0449        | <b>0.0210 ± 0.0454</b> |
| $V_{CH}$                 | 0.0273 ± 0.0562 | 0.0267 ± 0.0510 | 0.0220 ± 0.0480        | 0.0225 ± 0.0462        | 0.0214 ± 0.0449        | <b>0.0210 ± 0.0454</b> |
| $W_{max}$                | 0.0746 ± 0.0934 | 0.0685 ± 0.0862 | 0.0615 ± 0.0857        | 0.0592 ± 0.0796        | 0.0574 ± 0.0805        | <b>0.0569 ± 0.0806</b> |
| $W_{ortho}$              | 0.0780 ± 0.0950 | 0.0674 ± 0.0855 | 0.0708 ± 0.0877        | 0.0592 ± 0.0771        | <b>0.0567 ± 0.0752</b> | 0.0603 ± 0.0783        |
| Chamfer Distance         | 0.0941 ± 0.0795 | 0.0891 ± 0.0770 | <b>0.0821 ± 0.0707</b> | 0.0872 ± 0.0652        | 0.0864 ± 0.0652        | 0.0862 ± 0.0649        |

The ablation shows that the individual additions affect different aspects of the generated aneurysms. Morphology conditioning gives the lowest paired Chamfer distance, while prior-path calibration substantially improves the main size descriptors. SynVA-A1 gives the lowest height and orthogonal-width errors, and remains close to the best model for the other morphology measures. Therefore,

we select SynVA-A1 as the final model because it provides the most balanced trade-off across the evaluated criteria. It is the only variant that combines local vessel–ostium conditioning, morphology conditioning, geometry-aware ostium supervision, and prior-path calibration, and it avoids optimizing for a single descriptor at the expense of the overall generated shape. The stronger ostium variant slightly improves surface-area, volume, and maximum-width errors, but the increased interface emphasis led to sharper and more locally jagged surfaces in visual inspection. Thus, SynVA-A1 is selected as the best compromise between global sac shape, morphology control, and stable ostium attachment, rather than as the model with the largest number of row-wise best values.

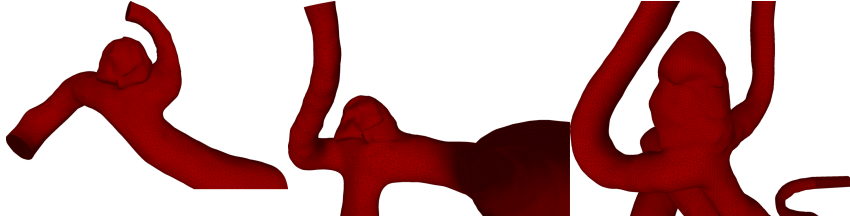


Figure 8: Representative SynVA-A1 failure cases.

Qualitatively, the generated pouches usually attach to the prescribed ostium, but representative failure cases can still exhibit sharp edges and locally jagged surfaces.

## F SynVA-A2

MeshAnything and MeshAnything V2 are designed to generate triangle meshes from complete 3D inputs, such as point clouds, which already implicitly encode the full target geometry [9, 10]. This paradigm is not directly applicable to anatomy-driven aneurysm synthesis, where the aneurysm geometry must be generated de novo from a pre-existing vessel without access to its full shape representation.

To address this limitation, we adopt the core autoregressive mesh decoding framework of MeshAnything V2 and extend it to support localized, conditional generation from partial geometric context. Specifically, we introduce (i) ostium-aware prefix conditioning, where tokens corresponding to the ostium boundary are injected into the autoregressive sequence, and (ii) conditioning on incomplete point clouds, representing only the surrounding vessel geometry. During generation, conditioning embeddings derived from the point cloud are first used to initialize the transformer state, followed by forced decoding of the ostium prefix tokens. The model then autoregressively generates the aneurysm mesh conditioned on this partial context (see Figure 9).

This formulation enables mesh synthesis that is spatially anchored to existing structures, allowing aneurysms to be generated directly from the ostium rather than requiring a full target shape as input. Consequently, our approach extends MeshAnything V2 from global shape reconstruction to structure-aware, incremental mesh generation, which is essential for anatomically consistent modeling. Further implementation details are provided below.

### F.1 Data Pre-processing

Both synthetic and real-world data are used for training and undergo an identical preprocessing pipeline. The following steps are therefore applied consistently across both datasets.

First, samples with aneurysm submeshes containing fewer than 80 faces are discarded to remove low-resolution and geometrically unreliable cases. To comply with the maximum input size of MeshAnything (1600 faces), aneurysm meshes exceeding this limit are simplified using quadric edge collapse. During this process, boundaries, normals, and topology are preserved to maintain geometric fidelity, with particular emphasis on retaining the ostium vertices.

To align the data with the model’s input assumptions, meshes are normalized and spatially standardized, depicted by the transformation step in Figure 9. Since MeshAnything V2 generates meshes within a unit cube  $[-0.5, 0.5]$  and the point cloud encoder operates on inputs in  $[-1, 1]$ , both aneurysm and vessel submeshes are transformed to ensure consistent scale, position, and orientation. As illustrated in Figure 9, the  $[-0.5, 0.5]$  bounding box is shown in blue, while the larger  $[-1, 1]$

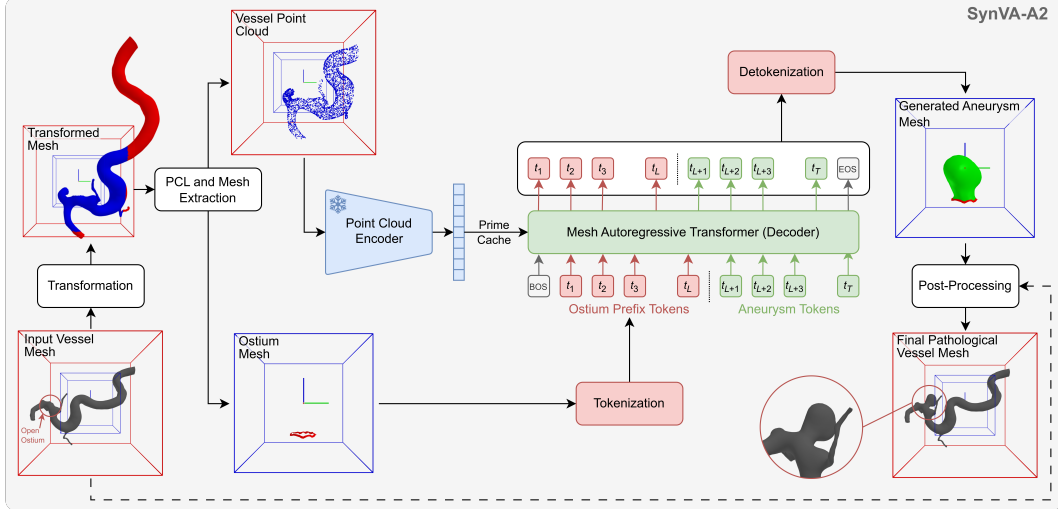


Figure 9: SynVA autoregressive aneurysm generation. A standardized healthy vessel is converted into an incomplete point cloud (conditioning) and an ostium mesh (prefix). Conditioned on both, a decoder-only transformer autoregressively generates aneurysm mesh tokens, enabling extrapolative growth from the ostium without requiring a full target shape. The output is detokenized, post-processed, and stitched back to the vessel.

region is depicted in red. Specifically, meshes are first translated such that the ostium centroid  $C_O$  coincides with the origin. They are then rotated so that the ostium normal vector aligns with the positive  $z$ -axis, enforcing a consistent growth direction. Subsequently, meshes are isotropically scaled such that the maximum ostium diameter  $N_{\max}$  is fixed to 0.25. Finally, meshes are translated by  $-0.3$  along the  $z$ -axis to better utilize the available generation space, as synthesis is restricted to the positive  $z$ -direction.

For prefix-based conditioning, an explicit ostium mesh is extracted from the vessel submesh by selecting all faces that contain at least one ostium vertex. This mesh represents the boundary ring from which the aneurysm is generated. To construct the conditioning input, the vessel submesh is spatially cropped around the ostium region within a fixed bounding box of  $[-1, 1]$ , under the assumption that distant structures have negligible influence on aneurysm shape. As shown in Figure 9, this corresponds to removing distal regions (red part of the transformed mesh) while retaining the local vessel neighborhood (blue part of the transformed mesh) for anatomically meaningful conditioning. From this cropped region, a point cloud of 20,000 surface samples is generated.

## F.2 Architecture

Building upon MeshAnything V2 [10], we introduce targeted conditioning mechanisms that enable mesh generation from partial geometric context, allowing aneurysm geometries to be synthesized directly from a pre-existing vessel. Specifically, our approach combines (i) conditioning on incomplete point clouds of the healthy vessel and (ii) explicit ostium-prefix token injection, enabling autoregressive mesh growth from a predefined boundary. This extends MeshAnything V2 from full-shape reconstruction to structure-aware, extrapolative mesh generation, which is essential for anatomically consistent aneurysm synthesis.

Both the vessel submesh (represented as a point cloud with normals) and the ostium prefix mesh serve as inputs. Meshes are first canonicalized and reordered, and subsequently tokenized using Adjacent Mesh Tokenization. Vertex coordinates are discretized with a resolution of 256 (instead of 128 in the original MeshAnything V2), as the lower resolution led to noticeable surface artifacts (staircasing) under our preprocessing. Consequently, pretrained weights are not used. The resulting token sequence consists of ostium prefix tokens, followed by aneurysm continuation tokens, and standard special tokens (BOS, EOS, padding).

The conditioning point cloud is encoded using a frozen pretrained ShapeVAE encoder [106], producing 257 tokens (one global and 256 local tokens) with a latent dimension of 768. The global token is projected to the transformer hidden size (1024), while each local token is concatenated with additional shape latents derived from the ShapeVAE bottleneck and projected via a linear layer. This design combines complementary geometric representations and improves the expressiveness of the conditioning signal. The final conditioning tensor has shape  $B \times 257 \times 1024$ , matching the hidden size of the ShapeOPT backbone (OPT-350M [104]).

The autoregressive model for mesh generation is a decoder-only transformer (OPT-350M) trained from scratch [104]. During training, the conditioning embeddings are provided as input embeddings, while the full token sequence (prefix + continuation) is teacher-forced. Crucially, loss masking is applied to the prefix tokens, such that optimization is restricted to the continuation, i.e., the aneurysm generation.

At inference time, the conditioning embeddings are first used to prime the transformer cache. A BOS token is inserted, after which the ostium prefix tokens are force-fed sequentially, ensuring that the subsequent generation is conditioned on the complete boundary. The aneurysm mesh is then generated autoregressively. To prevent degenerate early termination, EOS prediction is suppressed for a fixed number of steps following the prefix. Token selection is performed via argmax decoding. After removing special tokens, the predicted sequence is deterministically dequantized and detokenized into triangle meshes.

Post-processing removes invalid or low-quality outputs (e.g., meshes with fewer than 30 faces, prefix-only artifacts, or degenerate triangles based on normalized area and edge-length criteria). Standard mesh repair operations are applied, including removal of duplicate or unreferenced elements, non-manifold correction, and hole filling (up to a maximum size of 20). Normals are recomputed, and the mesh is transformed back into the original coordinate system via inverse normalization. Finally, the generated aneurysm is stitched to the vessel mesh. Ostium vertices are matched using a KD-tree followed by Hungarian assignment [40], and snapped to ensure exact alignment. The meshes are merged, duplicate vertices are consolidated (with label consistency), and the transition region is smoothed.

### F.3 Training Details

We adopt the same stratified and balanced data splits as used across all models in this work. Due to preprocessing constraints and additional validation checks (ensuring both point clouds and meshes lie within their respective bounding boxes), a small number of samples are excluded.

During training, data augmentation is applied to improve generalization while preserving geometric consistency between inputs and targets. All 3D assets—i.e., the conditioning point cloud, ostium prefix mesh, and aneurysm mesh—are jointly rotated around the z-axis to maintain spatial alignment. Additionally, mild simplex noise is applied exclusively to the aneurysm submesh to encourage robustness to local geometric variations. Ostium vertices are explicitly excluded from this perturbation, and a smooth transition is enforced in the surrounding region to avoid discontinuities at the vessel–aneurysm interface.

Training is performed with a batch size of 12 per GPU for up to 400 epochs. We employ the AdamW optimizer with weight decay 0.1 and mixed-precision (FP16) training. A cosine learning rate schedule with linear warm-up is used, starting from  $1 \times 10^{-6}$ . The base and final learning rates are set to  $1 \times 10^{-5}$  and  $6 \times 10^{-6}$  during base training, and reduced to  $1 \times 10^{-6}$  and  $6 \times 10^{-7}$  during fine-tuning. The maximum number of triangles is limited to 1600, and the coordinate discretization resolution is set to 256 (increased from 128 in the original MeshAnything V2). Training optimizes a masked next-token cross-entropy loss, where prefix tokens (i.e., ostium tokens) are excluded via loss masking, enforcing learning only on the continuation (aneurysm generation). During evaluation, we report the same loss in addition to Chamfer Distance and deviations in independently computed morphological parameters.

### F.4 Experimental Setting

We conduct three experiments under a unified training protocol. Due to the increased mesh discretization resolution (256 instead of 128), pretrained MeshAnythingV2 weights are not compatible.

Moreover, they are likely suboptimal for our setting, as we extend the task toward extrapolative mesh generation from incomplete point clouds, which differs fundamentally from the original full-shape reconstruction objective. Consequently, all models are trained from scratch.

Evaluation focuses on generalization to real anatomical geometries and is therefore always performed on the real-data test set. Since no separate validation split is available, validation is carried out on the respective training domain. However, to keep the process computationally tractable, validation is restricted to subsets and does not involve full mesh generation for all test samples. Final results are obtained independently by generating aneurysms for the complete test set using the selected model.

The experimental design covers three complementary regimes: (i) training purely on real data, (ii) training purely on synthetic data generated by the SynVA procedural model with cross-domain evaluation on real data, and (iii) synthetic pretraining followed by fine-tuning on real data using a reduced learning rate.

Model selection is based on a combination of validation loss, morphological parameter deviations (see Appendix B), and generation success rate. This setup enables a controlled analysis of real-only learning, synthetic-only generalization, and synthetic-to-real transfer, while maintaining a consistent and computationally efficient validation strategy.

To isolate the effect of point-cloud conditioning, we conduct an ablation in which both training (on synthetic data) and evaluation (on real data) are performed without point-cloud input.

## F.5 Additional Results

The results of the three experiments are summarized in this section. The configuration trained exclusively on real data is discarded, as the limited amount of available real samples is insufficient to effectively train the model, resulting in no valid mesh generations on the test set.

Table F.5 reports the mean absolute differences of independent morphological parameters with respect to the ground truth, as well as the Chamfer distance on the test set. For a fair comparison, only the intersection of successfully generated samples is considered ( $n = 46$ ).

Fine-tuning on real data consistently improves performance across all evaluated metrics. The validation loss decreases from 0.5592 (synthetic-only training) to 0.4636. While the success rate is slightly lower for the fine-tuned model (66%) compared to the synthetic-only model (68%), it produces more realistic geometries both quantitatively and qualitatively. Consequently, the fine-tuned model is denoted as SynVA-A2 and used for subsequent analyses. Representative failure cases are shown in Fig. 10, including remaining holes and, in rare cases, incomplete or only coarsely approximated aneurysm geometries.

Table 9: Comparison of SynVA-A2 training configurations based on the mean absolute differences of independent morphological aneurysm parameters and the Chamfer distance between generated and ground truth geometries.

| Mean Absolute Difference | Syn ( $n = 46$ )    | SynReal ( $n = 46$ )                  |
|--------------------------|---------------------|---------------------------------------|
| $A_A$                    | $0.3858 \pm 0.5941$ | <b><math>0.1998 \pm 0.3405</math></b> |
| $A_{CH}$                 | $0.3835 \pm 0.6023$ | <b><math>0.2040 \pm 0.3386</math></b> |
| $D_{max}$                | $0.1563 \pm 0.1587$ | <b><math>0.1004 \pm 0.1071</math></b> |
| $H_{max}$                | $0.1827 \pm 0.1668$ | <b><math>0.1059 \pm 0.1067</math></b> |
| $H_{ortho}$              | $0.1786 \pm 0.1591$ | <b><math>0.1032 \pm 0.1020</math></b> |
| $V_A$                    | $0.0671 \pm 0.1253$ | <b><math>0.0362 \pm 0.0662</math></b> |
| $V_{CH}$                 | $0.0604 \pm 0.1236$ | <b><math>0.0267 \pm 0.0584</math></b> |
| $W_{max}$                | $0.1080 \pm 0.1307$ | <b><math>0.0779 \pm 0.1042</math></b> |
| $W_{ortho}$              | $0.1001 \pm 0.1273$ | <b><math>0.0769 \pm 0.0969</math></b> |
| Chamfer Loss             | $0.1370 \pm 0.1095$ | <b><math>0.1054 \pm 0.0739</math></b> |

The ablation yields a 0% success rate on the real-data test set, as no aneurysm could be generated successfully. This result strongly supports the necessity of local point-cloud conditioning for autoregressive extrapolative generation in SynVA-A2 (adapted from MeshAnything V2 [10]). The t-SNE plot (Fig. 11) illustrates the distribution of generated and real aneurysms in latent space. While both models (A1 and A2) exhibit overlap with the ground-truth distribution, SynVA-A1 aligns more closely with real geometries than SynVA-A2.

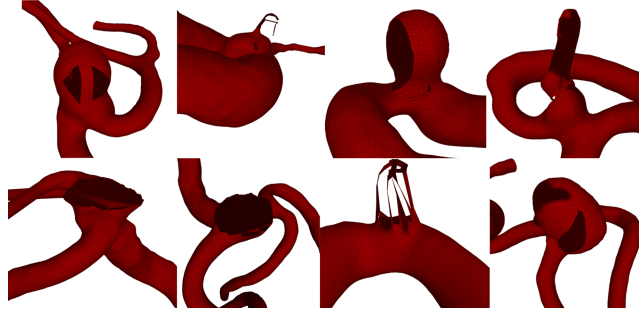


Figure 10: Qualitative examples of failure cases in ostium-conditioned aneurysm generation with SynVA-A2.

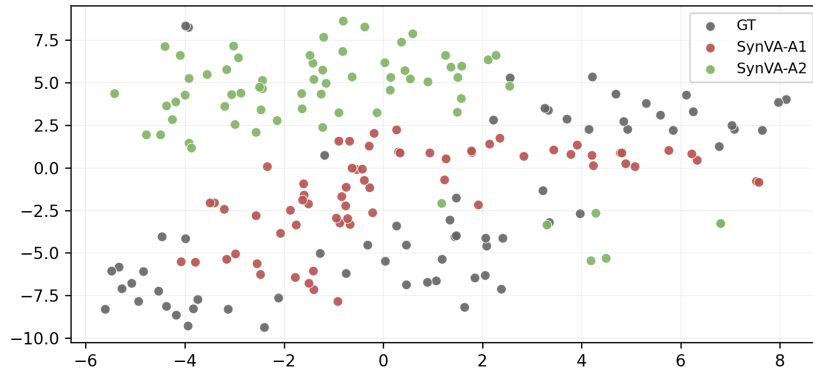


Figure 11: t-SNE embeddings of ground-truth and synthetic aneurysm meshes generated by SynVA-A1 and SynVA-A2.

## G SynVA-P1: Procedural Model

The SynVA-P1 procedural model is designed to generate parameterized meshes of vascular structures. By incorporating biological constraints, statistical measures derived from studies on real patient data, and stochastic variability, the model enables the controlled generation of a large number of diverse yet physiologically plausible vessel geometries. At its current stage, the model is limited to a single bifurcation of a parent vessel into two child vessels, along with the modeling of an aneurysm. Additional underlying assumptions are described in detail in the subsequent sections. Figure 12 illustrates the overall model and its individual components.

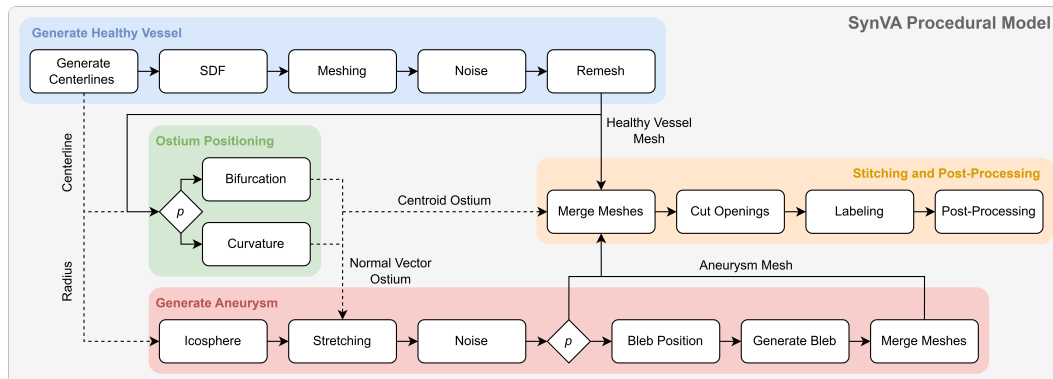


Figure 12: The SynVA procedural model for generating synthetic vessels with aneurysms. The main components are the healthy vessel generation (blue) and the aneurysm generation (red), which are linked by the ostium selection (green) and the stitching and post-processing (orange).

The first main component is the healthy vessel generation, which constructs the topology of a healthy vessel featuring a bifurcation without an aneurysm (see Appendix G.1). Subsequently, the centroid of the ostium—defined as the center of the intersection surface between the aneurysm and the healthy vessel—is determined within the ostium selection component (see G.2). In addition to the centroid, the corresponding surface normal is computed. The second main component of the SynVA procedural model is the conditional generation of the aneurysm pouch, guided by the previously determined ostium normal vector. A detailed description of the individual processing steps of this component is provided in Appendix G.3. The identified ostium centroid serves as the reference for the stitching process (Appendix G.4), in which both main components—the healthy vessel and the aneurysm—are merged using appropriate mesh operations. In addition, consistent labeling of the resulting structure as well as the computation of relevant morphological parameters are performed during this process. The model produces the following outputs:

- **Complete mesh:** A unified mesh representation of the vascular structure including the aneurysm, defined by vertices, faces, and associated surface normal (see Figure 13).
- **Vertex labels:** An index-based label file assigning each vertex a semantic class: 0 (healthy vessel), 1 (aneurysm), and 2 (ostium).
- **Point cloud:** A labeled point cloud representation of the complete vascular geometry, where class labels are encoded in the color attribute (see Figure 13).
- **Sub-point clouds:** Class-specific point clouds obtained by partitioning the full point set according to labels, resulting in separate point clouds for the healthy vessel, aneurysm, and ostium.
- **Sub-meshes:** Two sub-meshes corresponding to the healthy vessel and the aneurysm, respectively. Both sub-meshes share vertices at the ostium interface to facilitate consistent stitching and downstream processing.
- **Sub-mesh labels:** Index-based labels for each sub-mesh. For the healthy vessel sub-mesh, labels distinguish between vessel (0) and ostium (2), whereas for the aneurysm sub-mesh, labels distinguish between aneurysm (1) and ostium (2).
- **Additional outputs:** In addition to geometric representations and labels, the model provides the ostium centroid, the corresponding ostium normal vector, vessel centerlines with associated radii, and a set of derived morphological parameters (see Appendix B).

Example results from the SynVA-P1 procedural model can be seen in Figure 13. The model was tested on a NVIDIA GeForce RTX 4090 and a 13th Gen Intel Core i9-13900K CPU.

## G.1 Healthy Vessel Generation

The healthy vessel generation component constructs a closed vascular mesh featuring a single bifurcation and no aneurysms. It serves as the foundational geometry upon which subsequent processing steps are built. In the following, we first describe the underlying model design and then outline the corresponding parameter space exploration.

### G.1.1 Model Design

The healthy vessel generation component consists of five core steps that collectively generate a randomized vascular mesh with a single bifurcation (see Figure 12). The individual steps are described in the following.

**Generate Centerlines** In this step, parametric centerline splines and their associated radii are defined for the three vessel branches. The bifurcation point is initialized at the origin of the coordinate system. The parent vessel diameter  $d_0$  is then sampled uniformly at random from the interval  $[2, 4]$ . Based on  $d_0$ , the diameters of the two child vessels,  $d_1$  and  $d_2$ , are determined according to Murray’s law,

$$d_0^3 = d_1^3 + d_2^3, \quad (2)$$

which describes the physiological relationship between vessel diameters at a bifurcation [54]. To obtain a concrete parameterization, a random factor  $a \in [0.1, 0.9]$  is introduced, which defines the

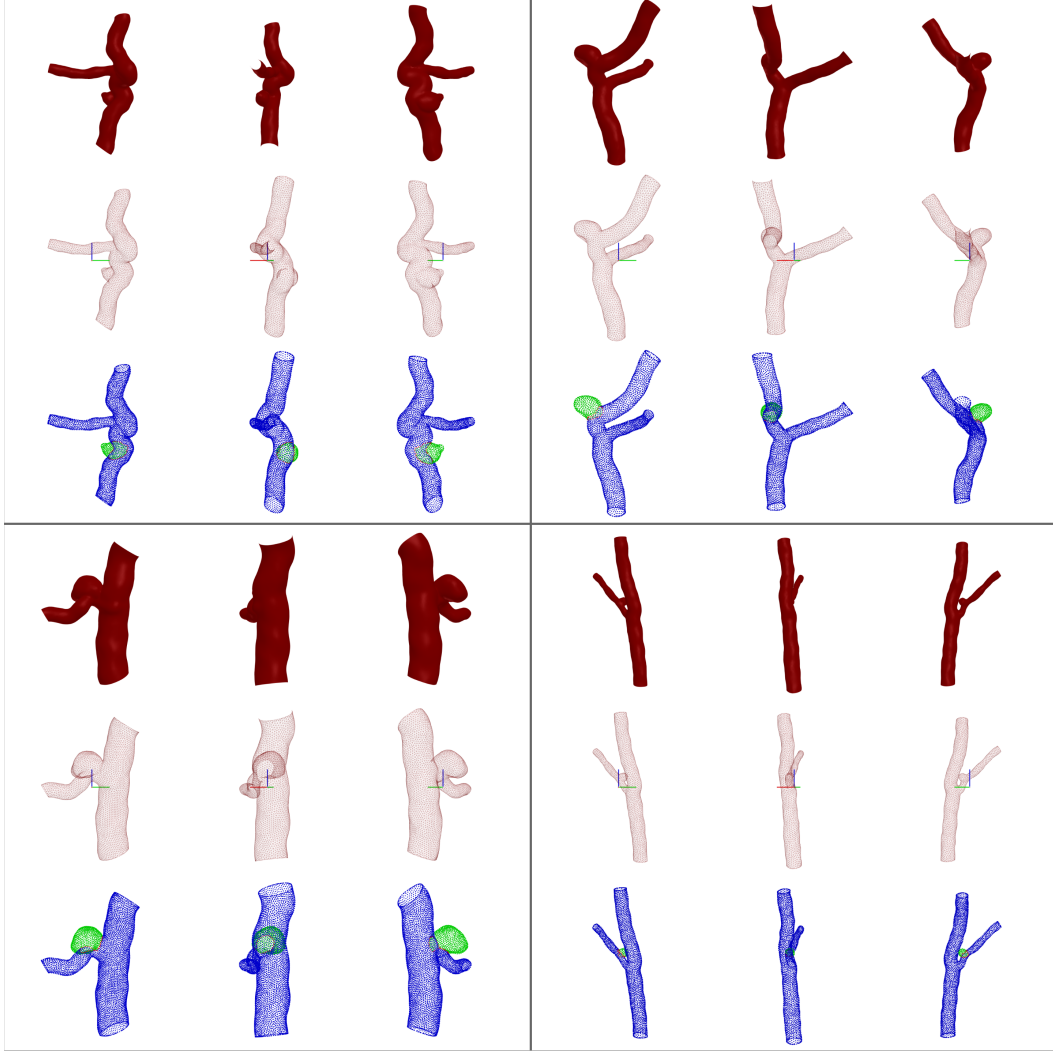


Figure 13: Qualitative examples of the SynVA procedural model. Four instances are visualized under different rotations, including mesh representations, wireframes, and labeled point clouds.

relative contribution of one child vessel with respect to the parent vessel in terms of volumetric flow. This yields

$$d_1 = \sqrt[3]{a \cdot d_0^3}, \quad (3)$$

$$d_2 = \sqrt[3]{d_0^3 - d_1^3}. \quad (4)$$

In addition to the vessel diameters, Murray's law further allows the derivation of the bifurcation angles  $\theta_1$  and  $\theta_2$ . These are computed as

$$\cos(\theta_1) = \frac{d_0^4 + d_1^4 - (d_0^3 - d_1^3)^{\frac{4}{3}}}{2d_0^2 d_1^2}, \quad (5)$$

$$\cos(\theta_2) = \frac{d_0^4 + d_2^4 - (d_0^3 - d_2^3)^{\frac{4}{3}}}{2d_0^2 d_2^2}, \quad (6)$$

following established formulations in the literature [44, 55, 65]. To ensure numerical stability, the arguments of the inverse cosine function are clipped to the interval  $[-1, 1]$  prior to applying arccos.

To introduce three-dimensional variability and determine the orientation of the vessel branches, a rotation-based formulation is employed. Specifically, three rotation matrices corresponding to rotations about the principal axes are defined as

$$\mathbf{R}_x = \begin{bmatrix} 1 & 0 & 0 \\ 0 & \cos(\text{tilt}_x) & -\sin(\text{tilt}_x) \\ 0 & \sin(\text{tilt}_x) & \cos(\text{tilt}_x) \end{bmatrix}, \quad (7)$$

$$\mathbf{R}_y = \begin{bmatrix} \cos(\text{tilt}_y) & 0 & \sin(\text{tilt}_y) \\ 0 & 1 & 0 \\ -\sin(\text{tilt}_y) & 0 & \cos(\text{tilt}_y) \end{bmatrix}, \quad (8)$$

$$\mathbf{R}_z = \begin{bmatrix} \cos(\text{rot}_z) & -\sin(\text{rot}_z) & 0 \\ \sin(\text{rot}_z) & \cos(\text{rot}_z) & 0 \\ 0 & 0 & 1 \end{bmatrix}. \quad (9)$$

These matrices are combined into a single rotation matrix

$$\mathbf{R} = \mathbf{R}_z \cdot \mathbf{R}_y \cdot \mathbf{R}_x. \quad (10)$$

The tilt angles  $\text{tilt}_x$  and  $\text{tilt}_y$  represent rotations around the  $x$ - and  $y$ -axes, respectively, and are sampled uniformly (in radians) from the interval  $[-10^\circ, 10^\circ]$ . The in-plane rotation  $\text{rot}_z$  is sampled uniformly from  $[0, 2\pi]$ . The direction of the parent vessel is defined along the negative  $z$ -axis as

$$\mathbf{d}_0 = [0 \quad 0 \quad -1]. \quad (11)$$

Given the bifurcation angles  $\theta_1$  and  $\theta_2$ , the initial (unrotated) direction vectors of the child vessels are defined in the  $xz$ -plane. Applying the combined rotation matrix  $\mathbf{R}$  yields the final direction vectors

$$\mathbf{d}_1 = \mathbf{R} \cdot [\sin(\theta_1) \quad 0 \quad \cos(\theta_1)], \quad (12)$$

$$\mathbf{d}_2 = \mathbf{R} \cdot [-\sin(\theta_2) \quad 0 \quad \cos(\theta_2)]. \quad (13)$$

For each direction vector, a randomized centerline curve is generated using a set of control points. The number of control points  $n_{\text{control}}$  is sampled uniformly from  $[5, 9]$ , the jitter parameter  $j$  from  $[0.7, 1.7]$ , and the total curve length  $l$  from  $[6, 14]$ . These parameter ranges were determined based on qualitative analysis; a systematic parameter space exploration is provided in Section G.1.2.

Starting from the bifurcation point at the origin, the curve is constructed by iteratively advancing along the previously defined direction vector. At each step, the local direction is updated based on the preceding direction, followed by smoothing and the addition of jitter to introduce controlled variability. To ensure anatomically plausible behavior near the junction, the jitter magnitude is modulated during the initial segment of the curve: specifically, for the first half of the control points, the jitter is scaled by a linearly increasing factor in the range  $[0.5, 1]$ . This enforces that the vessel initially follows the prescribed direction before gradually introducing curvature.

Given the resulting sequence of control points, a parametric spline is fitted to obtain a smooth centerline representation. The spline degree is defined as  $k = 3$ , and the curve is uniformly sampled at  $n = 120$  points with a smoothing factor of  $s = 0.3$ . The final output is a smooth centerline for each branch with an associated constant radius.

**SDF** We construct an implicit representation of the vascular geometry in the form of a signed distance function (SDF) based on the generated centerlines and their associated radii. Each centerline is interpreted as a piecewise linear curve (polyline), such that the vessel geometry is modeled as the continuous union of cylindrical segments with spherical end caps. For a query point  $\mathbf{p} \in \mathbb{R}^3$ , we first compute the minimal Euclidean distance to the closest centerline segment, ensuring a continuous and sampling-invariant approximation of the vessel structure. Subsequently, the corresponding vessel radius is subtracted, yielding the signed distance to the vessel surface. Formally, this defines an implicit function of the form

$$\phi(\mathbf{p}) = \min_k \left( \min_i \|\mathbf{p} - \mathbf{q}_{k,i}\| - r_k \right), \quad (14)$$

where  $\mathbf{q}_{k,i}$  denotes the closest point on segment  $i$  of centerline  $k$ , and  $\|\cdot\|$  is the Euclidean norm. The combination of multiple vessel branches is achieved via a pointwise minimum over the individual distance fields, corresponding to the union of their respective volumes. The resulting function  $\phi$  defines a signed distance field whose zero level set represents the vessel surface and can be directly used for subsequent mesh extraction.

**Meshing** The mesh is extracted from the previously computed signed distance field using the Marching Cubes algorithm [50]. The volumetric domain was bounded by  $[-20, 20]$  along each axis, and a grid resolution of 200 was chosen, providing a suitable trade-off between geometric fidelity and computational efficiency. The initial triangular mesh produced by Marching Cubes was subsequently cleaned to ensure geometric and topological consistency. This cleaning procedure comprises: merging vertices in close proximity, removing degenerate and duplicate faces as well as unreferenced vertices, and discarding any infinite or invalid values. Additionally, vertex normals were recomputed to guarantee correct surface orientation.

**Noise** Since the current mesh exhibits a uniform radius along each branch, we introduce geometric variability by iteratively superimposing noise at multiple scales and amplitudes relative to the local vessel radius. In our implementation, the number of noise iterations is set to 3. For each iteration, the noise scale increases proportionally to  $1/r$ , where  $r$  is the reference radius, while the noise amplitude for each scale is sampled randomly from a range between 0 and  $r/a_r$ . The reduction factor  $a_r$  is incremented for successive iterations to progressively decrease the amplitude of higher-frequency noise. The specific numerical ranges were determined empirically to produce visually plausible vessel geometries. For each scale and its associated amplitude, OpenSimplex noise is evaluated at the vertex positions, which are subsequently displaced along their normals. To mitigate artifacts arising from high-frequency displacement, a mild taubin smoothing filter is applied after each iteration [93]. This procedure produces a realistically perturbed mesh while maintaining overall topological consistency, enhancing the biological plausibility of synthetic vascular structures.

**Remesh** As the final step in the healthy vessel generation pipeline, the mesh is further refined using isotropic explicit remeshing, which improves the triangle size and aspect ratio across the surface. This procedure is conceptually inspired by Hoppe et al. [31] and ensures a more uniform and well-conditioned discretization suitable for subsequent processing.

The output of this fifth step is a closed, clean surface mesh representing the vascular geometry, including a single bifurcation. Together with the corresponding centerlines and idealized radii, this mesh forms the basis for all downstream components and analyses within the pipeline.

### G.1.2 Parameter Space Exploration

To assess the effects of individual parameters, a parameter space exploration was conducted. A fixed random seed was used to ensure that only the parameter under investigation varied, while all other parameters were held constant. Representative examples of relevant parameters for the healthy vessel model are shown in Figure 14.

It can be observed that increasing the parent vessel diameter  $d_0$  leads to a corresponding increase in the diameters of the child vessels. This behavior is governed by Murray’s law, which couples the vessel radii across bifurcations [54]. The variation of the factor  $a$  reveals two key effects. First, for small or large values of  $a$ , the diameters of the child vessels become increasingly asymmetric, whereas for  $a = 0.5$  the diameters are approximately equal. Second, the branching angles are also affected. This follows from the fact that Murray’s law links vessel diameters to optimal branching angles (see Equations 5 and 6). Increasing the number of control points  $n_{\text{control}}$  results in a more curved parent branch, as the underlying spline representation gains additional degrees of freedom. In contrast, increasing the jitter parameter  $j$  has only a minor effect on the overall trajectory, primarily introducing small local perturbations that are most noticeable towards the distal end of the parent branch. The parameter  $l$  controls the length of the parent branch while leaving the child branch lengths unchanged. Finally, the number of noise iterations directly affects the surface characteristics of the mesh. Without noise, the geometry exhibits a uniform thickness. As the number of noise iterations increases, the surface becomes progressively more irregular due to the superposition of noise functions at increasing scales.

## G.2 Ostium Positioning

Building upon the outputs of the healthy vessel generation, the ostium point is determined (see Figure 12). This point corresponds to a vertex on the surface mesh. Additionally, a normal vector is estimated, which can be interpreted as the initial growth direction of the aneurysm. With probability  $p = 0.5$ , the ostium point is located at the bifurcation, i.e., at the junction where the blood flow

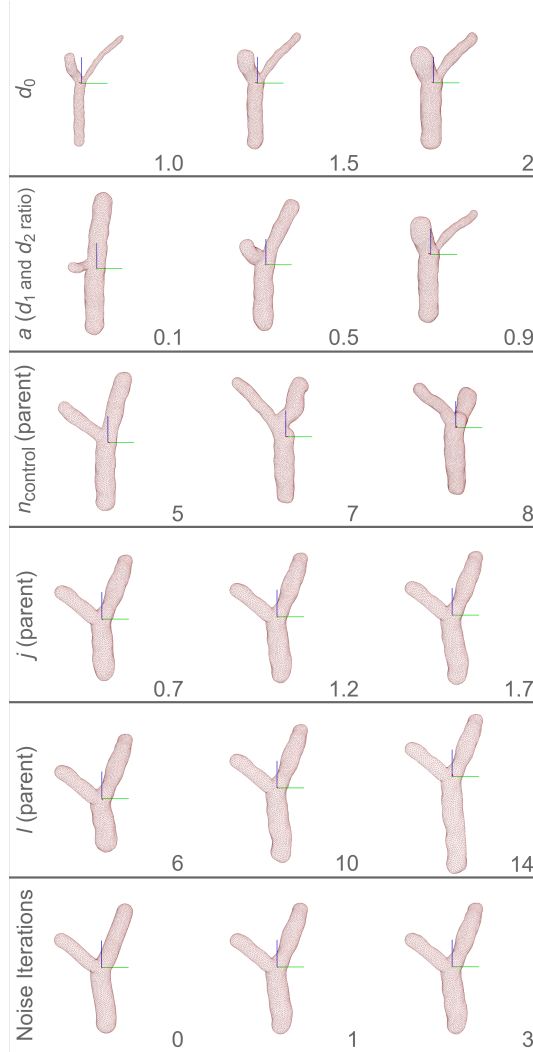


Figure 14: Parameter space exploration of the healthy vessel generation pipeline. Each row corresponds to a different parameter: the parent vessel diameter  $d_0$ , the branching ratio factor  $a$  defining the relative diameters of the child vessels, the number of control points  $n_{\text{control}}$ , the jitter amplitude  $j$ , the vessel length  $l$ , and the number of noise iterations. For each parameter, three representative values spanning the respective range are shown.

from the parent vessel splits into the two child vessels. This choice is motivated by the increased hemodynamic stress typically observed at such locations [22, 66, 72]. In the remaining cases, the ostium point is determined based on vessel curvature, reflecting the assumption that aneurysms are more likely to occur in highly curved regions than along straight vessel segments.

**Bifurcation** For the bifurcation-based selection, a local direction vector of the parent branch at the junction is first estimated by averaging the direction vectors of the first five centerline points. This vector approximates the flow direction towards the bifurcation. Next, the surface curvature of the mesh is computed using the algebraic point set surfaces (APSS) method on a per-vertex basis [27, 28]. Within a predefined search radius around the junction point, all vertices and their associated surface curvatures are evaluated. The selected ostium point is the vertex with minimal curvature that deviates by at most  $45^\circ$  from the estimated direction vector. The corresponding normal vector is then defined as the normalized vector between the junction point and the selected surface vertex.

**Curvature** For curvature-based selection, the centerline curvature is first computed from the gradients of the spline points and multiplied by the local radius to obtain a scalar score. The point with the maximum score is selected, excluding regions within a safety margin near the ends of the centerline to avoid anatomically implausible placements. Within a predefined search radius relative to the vessel radius, the surface vertices are evaluated based on their curvature. Surface curvature is computed analogously to the bifurcation case. In 90 % of cases, the vertex with maximal curvature (i.e., outward-facing) is selected, reflecting regions of increased hemodynamic wall stress, which have been associated with aneurysm formation and are also observed in clinical data. In the remaining 10 % of cases, however, the vertex with minimal curvature (i.e., inward-facing) is chosen. This accounts for clinically observed scenarios in which aneurysms occur opposite to the primary curvature of the vessel, such as in the internal carotid or ophthalmic artery (e.g., [79, 100]). The adopted sampling strategy was qualitatively validated against real clinical data to ensure plausible spatial distributions. The normal vector is then defined as the normalized vector between the selected surface vertex (ostium point) and the corresponding centerline point.

The three cases—bifurcation-based, outward curvature-based, and inward curvature-based selection—are illustrated in Figure 15.

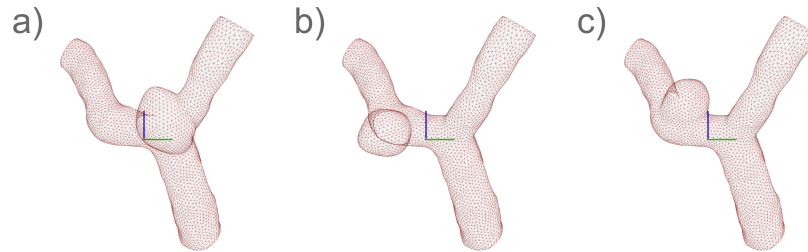


Figure 15: The three ostium location strategies of the SynVA procedural model. a) Placement at the bifurcation, b) placement at a location of maximal surface curvature, and c) placement at a location of minimal surface curvature.

### G.3 Aneurysm Generation

The aneurysm generation component constructs a closed aneurysm mesh conditioned on the ostium normal vector and the local vessel radius. It builds upon the previously defined geometric context to ensure coherent integration with the vascular structure. In the following, we first describe the underlying model design and then outline the corresponding parameter space exploration.

#### G.3.1 Model Design

Das Modell zur Erstellung des Aneurysma Meshes besteht im kern aus 6 Schritten (siehe Abbildung 13. Die einzelnen Schritte sind nachfolgend aufgeführt.

**Icosphere** In the first step, an icosphere with four subdivisions is generated using a prescribed radius. This radius is defined as the vessel radius at the previously determined ostium location, scaled by a random factor in the range  $[0.8, 2.0]$ . This formulation introduces controlled variability in aneurysm size while maintaining a consistent relationship to the underlying vessel geometry.

**Stretching** In the second step, the mesh is anisotropically stretched along the previously determined normal vector. The stretching is performed via a directional scaling operation, where each vertex is displaced proportionally to its projection onto the normalized direction vector. The stretch magnitude is controlled by a factor sampled uniformly from the range  $[0, 0.7]$ , resulting in elongation along the normal direction while preserving the orthogonal structure of the mesh.

**Noise** Subsequently, the mesh is iteratively perturbed using OpenSimplex noise with varying scales and amplitudes. The implementation follows the noise formulation introduced in the healthy vessel generation and is therefore not described in further detail.

**Bleb Position** With probability  $p = 0.3$ , a bleb—defined as a localized surface bulge—is added to the aneurysm geometry. Bleb formation is clinically relevant, as it is associated with an increased risk of rupture. This design choice is motivated by Salimi Ashkezari et al. [70], who report the presence of one or multiple blebs in 36 % of cases. In the current procedural SynVA model, we restrict the generation to a single bleb. To determine the centroid of the bleb on the aneurysm surface, a ray is cast from the mesh centroid in the direction of the ostium normal vector, and the corresponding surface intersection point is identified. Within a predefined local search region around this intersection, a vertex is randomly selected and defined as the bleb centroid. The associated normal vector of the bleb is then computed as the normalized vector between the mesh centroid and the selected bleb centroid.

**Generate Bleb** The bleb itself is generated analogously to the aneurysm base shape. Instead of using the ostium centroid and normal vector, the bleb centroid and its corresponding normal vector are employed to guide the mesh transformation. The bleb radius is scaled by a factor randomly sampled from the range  $[0.2, 0.4]$ , introducing controlled variability in bleb size relative to the parent aneurysm.

**Merge Meshes** In the sixth and final step of the aneurysm mesh generation, the aneurysm mesh is merged with the bleb mesh. The bleb is first translated to align with the bleb centroid. A mesh cleaning operation is then performed (as previously described), followed by a boolean union of the meshes, which is accompanied by remeshing, additional cleaning, and Laplacian smoothing. The output of the aneurysm generation pipeline is thus a finalized aneurysm mesh, either with or without an attached bleb.

### G.3.2 Parameter Space Exploration

To assess the effects of individual parameters, a parameter space exploration was conducted. A fixed random seed was used to ensure that only the parameter under investigation varied, while all other parameters were held constant. Representative examples of relevant parameters for the aneurysm model are shown in Figure 16.

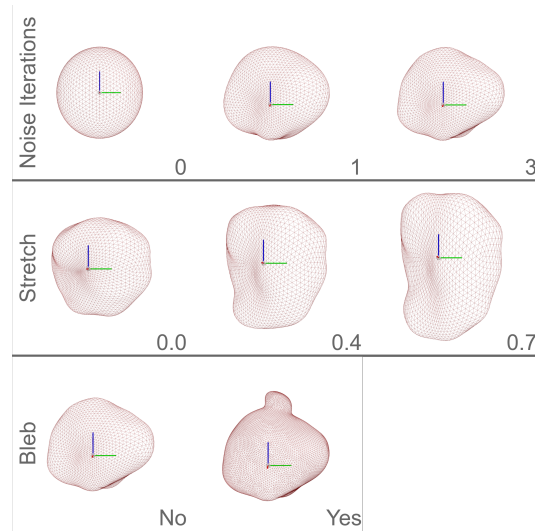


Figure 16: Parameter space exploration of the aneurysm generation pipeline. Each row corresponds to a different parameter: the noise iterations, the stretching factor and presence or absence of a bleb.

It can be observed that increasing the number of noise iterations from 1 to 3 primarily introduces finer surface perturbations. The effect of stretching along the normal vector, here aligned with the blue  $z$ -axis, is pronounced, resulting in substantial mesh deformation. The bleb is added in the positive direction of the corresponding normal vector.

## G.4 Stitching and Post-processing

The stitching and postprocessing stage constitutes the final component of the pipeline, combining the two meshes and preparing them for storage in a standardized data structure. This stage consists of four sequential steps, described below.

**Merge Meshes** This step is largely analogous to the merging procedure used for combining the aneurysm and bleb meshes. Here, the aneurysm is first translated to align with the ostium centroid. A boolean union is then performed with the healthy vessel and aneurysm, followed by remeshing, mesh cleaning, and Laplacian smoothing. The resulting mesh represents the pathological vessel.

**Cut Openings** Since the generated mesh remains watertight, it is opened in this step to enable downstream applications such as fluid simulations. To this end, the terminal endpoints of each centerline branch are identified, representing the inlet and outlet locations of the vessel. For each branch, a local cutting operation is performed. Specifically, a tangent vector at the selected endpoint is used to define a cutting plane, whose normal is aligned with the outward vessel direction. A local submesh is then extracted within a radius of  $2r$  around the endpoint, and the slicing operation is applied exclusively to this region. This localized processing ensures that only the intended vessel openings are created while preserving surrounding geometry. After slicing, the modified local region is recombined with the unaffected remainder of the mesh. A mesh cleaning step (as described previously) and normal correction are subsequently applied.

**Labeling** Although the aneurysm and vessel submeshes are known from the generation process, the preceding merging and remeshing operations no longer preserve any explicit vertex correspondence. Consequently, vertex labels must be recomputed. To this end, a ray-casting-based approach is employed, which proved to be robust in practice. For each vertex of the pathological vessel mesh, a ray is cast from the aneurysm centroid toward the vertex. The first intersection of this ray with the aneurysm surface is determined and compared to the Euclidean distance between the centroid and the respective vertex. If both distances agree within a tolerance threshold, defined relative to the aneurysm size, the vertex is classified as belonging to the aneurysm surface. In cases where the ray-intersection procedure fails, a fallback strategy based on nearest-neighbor queries using a  $k$ -d tree is applied. Specifically, vertices are labeled as aneurysm if their distance to the aneurysm mesh falls below the same tolerance. Empirically, this method was found to be less accurate than the ray-casting approach. After the initial binary classification into vessel and aneurysm vertices, ostium vertices are identified. A vertex is labeled as ostium if it belongs to the aneurysm class and is connected via mesh edges to at least one vessel vertex, thereby marking the interface between both structures. Finally, a set of consistency checks and corrective operations is applied to ensure label coherence. These include, for example, the removal of isolated misclassified vertices and the enforcement of a consistent ostium topology, such that the interface forms a well-defined boundary between aneurysm and vessel.

**Post-processing** In the final step of the SynVA procedural model (see Figure 12), additional consistency checks are performed to identify and discard invalid samples. Specifically, it is verified whether a single coherent ostium ring is present and whether the number of ostium vertices exceeds a minimal threshold. If these conditions are not met, the aneurysm is regenerated; after multiple unsuccessful attempts, the healthy vessel geometry is also resampled. Following validation, the aneurysm neck region is locally smoothed around the ostium vertices using Taubin smoothing to ensure a geometrically consistent and smooth transition between vessel and aneurysm. The mesh is then normalized to the range  $[-1, 1]$ , and a labeled point cloud is extracted from the mesh vertices. Additionally, separate sub-point clouds are generated for each label class. Subsequently, the ostium centroid and its associated normal vector are recomputed based on the ostium vertices. This is achieved by estimating the center of mass and fitting a local plane to the ostium region. This recomputation is necessary, as the irregular geometry of the aneurysm can introduce deviations from the initial ostium estimation. Finally, separate submeshes for the vessel and aneurysm are extracted, and a set of morphological parameters, described in Section B, is computed. All outputs are then stored in a standardized data structure for downstream processing.

## H Dataset

The proposed SynVA-P1 procedural model enables the scalable generation of arbitrarily large datasets of labeled vascular meshes, including corresponding point clouds and auxiliary information. Such data can be directly utilized for training and evaluating downstream tasks. In addition to our model code, we provide a pre-generated SynVA dataset comprising 50,000 synthetic vessel samples, allowing immediate use without requiring execution of the procedural pipeline. Representative examples are shown in Figure 13. To further characterize the dataset, summary statistics of the morphological parameters are reported in Figure 17, providing insights into its structural variability and distribution of the aneurysms.

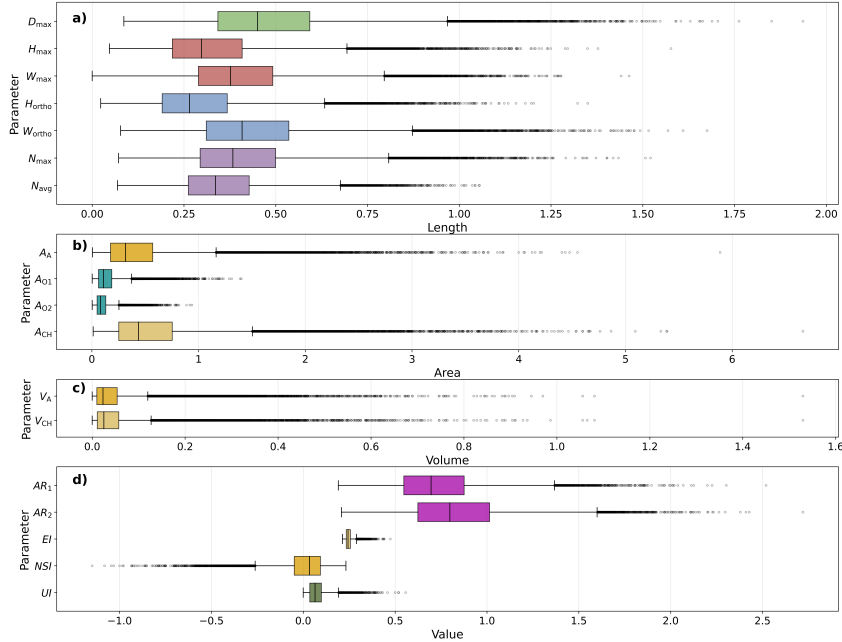


Figure 17: Distribution of morphological parameters across the SynVA procedural dataset, illustrated as boxplots over the sampled parameter space. The parameters are grouped into four categories: a) length-based metrics, b) surface area measures, c) volumetric measures, and d) ratios and derived indices.

Across all subplots, a concentration of samples within characteristic value ranges can be observed, accompanied by a non-negligible number of outliers. This indicates both consistency and variability in the generated dataset, highlighting the diversity of the procedural model.

For the length-based parameters (Figure 17a), aneurysms exhibit consistently smaller heights ( $H_{\max}$  and  $H_{\text{ortho}}$ ) compared to their corresponding widths ( $W_{\max}$  and  $W_{\text{ortho}}$ ), suggesting predominantly laterally expanded geometries. In addition, the ostium-related measures ( $N_{\max}$  and  $N_{\text{avg}}$ ) indicate relatively large neck extents, implying that aneurysms in the dataset tend to have broad necks rather than strongly constricted ones.

Regarding surface areas (Figure 17b), the aneurysm area  $A_A$  and its convex hull counterpart  $A_{CH}$  lie within similar value ranges, with  $A_{CH}$  being consistently larger due to its enclosing definition. In contrast, the ostium areas ( $A_{O1}$  and  $A_{O2}$ ) are comparatively small and exhibit low variance.

For volumetric measures (Figure 17c), only minor differences between  $V_A$  and  $V_{CH}$  are observed. This can be attributed both to their inherent geometric similarity and to the employed fallback strategy, where  $V_{CH}$  is used when  $V_A$  cannot be reliably computed due to incomplete closure of the ostium.

Finally, the ratio-based and shape descriptors (Figure 17d) show that  $AR_1$  and  $AR_2$  occupy similar value ranges. The ellipticity index ( $EI$ ) is concentrated within a narrow interval, whereas the non-sphericity index ( $NSI$ ) and undulation index ( $UI$ ) exhibit broader distributions. It should be noted that, similar to the volumetric measures, the fallback strategy for  $V_A$  may introduce bias into  $NSI$  and  $UI$ .

## H.1 Responsible AI Information

This section provides Responsible AI (RAI) information for the released SynVA-P1 dataset, covering data limitations, data biases, personal or sensitive information, data use cases and construct validity, and social impact, as well as dataset provenance, including source datasets and data generation processes.

**Data limitations** The SynVA procedural dataset is a fully synthetic dataset of 3D pathological vascular meshes generated by the rule-based procedural model SynVA-P1. The generated samples are designed to be anatomically and morphologically plausible, but they do not represent the full variability of patient-level cerebrovascular anatomy, vessel-structure variants, demographic populations, acquisition protocols, or rare aneurysm morphologies. The procedural model supports only simplified bifurcating configurations, so the dataset is not suitable for studying anatomical cases outside this model class or for drawing conclusions about clinical prevalence or population-level distributions. The dataset is not validated to reproduce true hemodynamic quantities such as wall shear stress or pressure fields, and it should not be used as a substitute for clinical measurements or patient-derived imaging data. Some meshes may require additional quality control and preprocessing before CFD or other physics-based analyses.

**Data biases** The SynVA procedural dataset is generated using a rule-based procedural model (SynVA-P1) that encodes physiological assumptions (e.g., Murray’s law), statistical priors from selected studies, and geometric construction rules. As a result, the dataset may reflect inductive biases toward simplified, idealized vascular structures, including a focus on local tree-like vessel geometries and bifurcating configurations. This can lead to selection and representation biases, where common or well-characterized anatomical patterns are over-represented, while complex vessel topologies, rare aneurysm morphologies, and atypical anatomical variants are under-represented or absent. Because the dataset is fully synthetic, it does not capture biases arising from clinical acquisition pipelines (e.g., imaging modality, reconstruction artifacts, or annotation variability), but instead introduces model-driven biases determined by the design choices, parameter distributions, and source studies used to construct the procedural generator. These biases may affect downstream model behavior, particularly when models are applied to real patient data, different demographic populations, or clinical settings not reflected in the underlying assumptions. Users should exercise caution when using SynVA for training or benchmarking, especially in contexts requiring generalization to underrepresented anatomical variants, rare aneurysm shapes, or real-world clinical data distributions, as performance estimates may be overly optimistic or not transfer reliably.

**Personal or sensitive information** The SynVA procedural dataset does not contain any real patient data and is fully synthetically generated using a rule-based procedural model (SynVA-P1). As such, it does not include personal or sensitive information such as gender, age, ethnicity, socio-economic status, geographic origin, health records, or any other identifiable or protected attributes. However, the dataset may implicitly reflect aggregate statistical properties or assumptions derived from prior studies used to parameterize the procedural model. These do not correspond to identifiable individuals or specific demographic groups, and no direct inference about real populations or individuals should be made based on this dataset.

**Data use cases** The SynVA procedural dataset is designed to represent anatomically and morphologically plausible vascular geometries with aneurysms, generated via a rule-based procedural model (SynVA-P1). The dataset provides consistent geometric structure and dense semantic labels (vessel, aneurysm, ostium), making it suitable for tasks where the underlying construct is geometric and morphological representation of vascular anatomy, rather than patient-specific physiology or clinical outcomes. Construct validity is therefore established for use cases such as: synthetic 3D vascular mesh generation, anatomy-conditioned aneurysm synthesis and editing, semantic segmentation on meshes or point clouds, morphology analysis, and simulation-oriented preprocessing workflows. The dataset is also appropriate for method development and evaluation, including pretraining, data augmentation, controlled benchmarking, robustness testing, and exploratory studies, particularly in settings where real annotated aneurysm datasets are limited. Construct validity is not established for tasks that depend on accurate patient-specific or population-level clinical realism, including hemodynamic prediction (e.g., wall shear stress, pressure fields), rupture-risk estimation, disease progression modeling, or clinical decision-making. Accordingly, the dataset should not be used as standalone

evidence for diagnosis, treatment planning, prognosis, regulatory evaluation, or deployment in clinical decision-support systems without extensive validation on real-world clinical data.

**Social impact** The SynVA procedural dataset may have positive societal impact by enabling research on intracranial aneurysm analysis in settings where real, well-annotated medical data are scarce or difficult to access due to privacy constraints. By providing large-scale, labeled synthetic vascular meshes, the dataset can support the development and benchmarking of methods for vascular geometry generation, segmentation, morphology analysis, aneurysm editing, and simulation-oriented preprocessing workflows. In the long term, such tools may strengthen research infrastructure in cerebrovascular disease modeling and help reduce reliance on sensitive patient data. However, negative impacts and misuse risks exist. Because the dataset is synthetic and optimized for anatomical and morphological plausibility rather than clinical or hemodynamic validation, there is a risk that it could be mistakenly treated as equivalent to real patient data. This may lead to inappropriate use in clinical contexts such as diagnosis, treatment planning, rupture-risk prediction, or patient-specific prognosis without sufficient validation on real-world data. Fairness risks may arise from the procedural generation process, which is based on simplified physiological assumptions and statistical priors. As a result, certain anatomical variants, rare aneurysm morphologies, demographic groups, geographic populations, or imaging conditions may be underrepresented or absent, potentially leading to biased downstream models if not carefully addressed. Mitigations include clearly documenting the synthetic nature of the dataset, restricting its recommended use to research and benchmarking contexts, explicitly reporting known data limitations and model assumptions, and encouraging validation on real clinical datasets before any downstream deployment. Additional safeguards include applying quality control and preprocessing when using the data in simulation or learning pipelines, and avoiding unsupported clinical or high-stakes applications.

**Synthetic data** True. The SynVA procedural dataset is fully synthetically generated.

**Source datasets** None. The SynVA dataset is not derived from any existing dataset. It is generated entirely using a rule-based procedural model (SynVA-P1) based on physiological principles (e.g., Murray’s law) and statistical findings reported in prior studies. These studies are cited in the accompanying paper. The full procedural generation model, including all rules, assumptions, and parameterizations, is described in detail in the appendix, ensuring transparency and reproducibility of the dataset creation process.

**Provenance activities** Each sample in the SynVA dataset was generated independently by sampling a bifurcating vessel geometry, selecting an ostium according to the procedural placement strategy, synthesizing an aneurysm sac conditioned on the ostium location, normal direction, and local vessel radius, and stitching the aneurysm to the vessel surface. The generation process uses physiological constraints, statistical priors, and stochastic geometric perturbations. For preprocessing, a standardized pipeline was applied to the SynVA-P1 outputs. This includes normalizing mesh coordinates, extracting labeled point clouds and sub-point clouds, computing ostium centroids and normals, extracting sub-meshes, and computing morphological parameters. The resulting datapoints contain complete vessel–aneurysm meshes with vertex-wise labels for vessel, aneurysm, and ostium regions, along with derived point clouds, submeshes, centerline and radius information, ostium descriptors, and morphological parameters. For annotation, labels are produced automatically by the synthetic generation pipeline. The labeling schema marks mesh regions as healthy vessel, aneurysm, or ostium. No human annotation instructions or inter-annotator agreement scores are applicable to the SynVA-P1 labels because they are generated procedurally.

## I Downstream Task: Aneurysm Head Identification

To evaluate the practical value of the generated synthetic vascular data, we use aneurysm head identification as a downstream task. The task is formulated as a semantic segmentation problem, where each point in the vascular structure is classified as vessel, aneurysm, or ostium. This setup allows us to assess whether synthetic data can support training and generalize to real test cases.

## I.1 Architecture

For the aneurysm head identification task, we used a point-wise semantic segmentation model based on Point Transformer V3 (PTv3) [99], implemented within the Pointcept framework [60]. PTv3 was selected because it is designed for efficient and scalable point cloud processing, making it suitable for vascular geometries represented as 3D point clouds. The downstream task was formulated as a three-class semantic segmentation problem. For each input point, the model predicts one of three anatomical labels: vessel, aneurysm, or ostium. The input to the network consisted of six channels, corresponding to the 3D point coordinates and surface normals.

The PTv3 backbone follows an encoder and decoder structure similar to a U-Net architecture. The encoder progressively downsamples the point representation while increasing the feature dimension from 32 to 512 channels. The decoder then restores the point resolution through unpooling and skip connections, reducing the feature representation back to 64 channels before classification. Each transformer block uses serialized self-attention, residual connections, pre-normalization, sparse convolution based positional encoding, and a feed-forward MLP. PTv3 handles unordered point clouds by serializing points into structured sequences using different space filling curve orderings. In our configuration, Z order, transposed Z order, Hilbert order, and transposed Hilbert order were used, with order shuffling enabled during training. This allows the model to capture spatial relationships from different ordering perspectives. The final model contained 46.17 million trainable parameters.

## I.2 Training Details

For the downstream task, we use PTv3 across all experiments and vary only the training data regime to assess the impact of synthetic data. Real and synthetic datasets follow the same train/test splits as defined in this work.

Point clouds are preprocessed using grid sampling with a voxel size of 0.01 and centered to ensure a consistent spatial representation. During training, data augmentation is applied to improve robustness: random point dropout (ratio 0.2, probability 0.2), random rotations around the  $z$ -axis in  $[-1, 1]$  (probability 0.5), small rotations around  $x$  and  $y$  in  $[-0.015, 0.015]$  (probability 0.5 each), random scaling in  $[0.9, 1.1]$ , random flipping (probability 0.5), and Gaussian jittering with  $\sigma = 0.005$  (clipped at 0.02). Validation is performed without stochastic augmentation.

In total, 11 experiments are conducted. Five models are trained from scratch on real data using 10%, 25%, 50%, 75%, and 100% of the available training set, corresponding to 67, 166, 331, 497, and 662 samples, respectively. For each setting, 10% of the selected subset is used for validation and 90% for training. In addition, five models are first pretrained on the full synthetic training set (40,000 samples generated with SynVA-P1, with 10,000 synthetic samples used for validation) and subsequently fine-tuned on the same real-data subsets. Finally, one model is trained exclusively on synthetic data. No joint mixed-batch training is performed, allowing a clear analysis of the individual contributions of synthetic and real data. All models are evaluated on the same real test set of 100 samples.

Training is performed for 100 epochs using AdamW. A batch size of 4 is used in all settings except for the 100% real-data experiment, where a batch size of 6 is feasible. The base learning rate is set to  $5 \times 10^{-4}$ , with a reduced rate of  $5 \times 10^{-5}$  for transformer block parameters. Weight decay is 0.05, and a OneCycleLR schedule with cosine annealing is applied. Gradients are clipped at a maximum norm of 1.0, and training uses bfloat16 mixed precision. The PTv3 backbone employs stochastic depth with  $\text{drop\_path} = 0.3$ .

The loss function combines cross-entropy and Lovász loss with equal weighting, using an index ignoring of  $-1$ . This setup balances point-wise classification accuracy and segmentation overlap, which is particularly important for smaller structures such as aneurysm and ostium. Evaluation is performed using mean Intersection over Union (mIoU), mean class accuracy (mAcc), overall accuracy (allAcc), and per-class IoU and accuracy for vessel, aneurysm, and ostium.

All experiments are conducted on a single NVIDIA A100 (80GB PCIe) GPU and an Intel Xeon Gold 6330 CPU.

### I.3 Results

The quantitative results of the downstream aneurysm head identification task, used to assess the usefulness of the procedurally generated SynVA-P1 dataset (50,000 samples), are summarized in Table 10 across all 11 training configurations.

Table 10: Quantitative evaluation of point-wise semantic segmentation performance for aneurysm head separation on the held out real test set. Metrics are reported in percent.

| Training data                           | mIoU $\uparrow$ | mAcc $\uparrow$ | allAcc $\uparrow$ | Vessel IoU $\uparrow$ | Aneurysm IoU $\uparrow$ | Ostium IoU $\uparrow$ |
|---|-----------------|-----------------|-------------------|-----------------------|-------------------------|-----------------------|
| 10 % real data                          | 50.41           | 55.52           | 96.72             | 96.73                 | 51.35                   | 3.16                  |
| 25 % real data                          | 60.66           | 73.33           | 98.21             | 98.51                 | 77.49                   | 5.97                  |
| 50 % real data                          | 63.79           | 80.06           | 98.61             | 98.89                 | 84.31                   | 8.17                  |
| 75 % real data                          | 64.13           | 83.22           | 98.61             | 98.96                 | 84.44                   | 9.00                  |
| 100 % real data                         | 64.84           | 84.95           | 98.66             | 98.98                 | 86.22                   | 9.33                  |
| Synthetic pretraining + 10 % real data  | 63.88           | 78.35           | 98.67             | 98.90                 | 82.94                   | 9.80                  |
| Synthetic pretraining + 25 % real data  | 66.42           | 82.23           | 98.99             | 99.18                 | 88.58                   | 11.49                 |
| Synthetic pretraining + 50 % real data  | <b>67.11</b>    | 86.10           | <b>99.03</b>      | <b>99.29</b>          | <b>89.24</b>            | 12.82                 |
| Synthetic pretraining + 75 % real data  | 66.50           | 85.52           | 98.93             | 99.17                 | 88.81                   | 11.52                 |
| Synthetic pretraining + 100 % real data | 66.93           | <b>87.86</b>    | 98.95             | 99.20                 | 88.45                   | <b>13.13</b>          |
| 100 % synthetic data                    | 36.78           | 42.09           | 92.24             | 92.15                 | 17.80                   | 0.38                  |

The results indicate that synthetic pretraining consistently improves downstream performance across all real-data fractions. For the 10 % real-data setting, the real-only model achieves an mIoU of 50.41, whereas synthetic pretraining followed by fine-tuning on the same fraction increases mIoU to 63.88. Similar gains are observed for 25 %, 50 %, 75 %, and 100 % real data, indicating that the synthetic dataset provides useful geometric priors, especially in low-data regimes.

The best overall mIoU is obtained with synthetic pretraining followed by fine-tuning on 50 % real data, reaching 67.11. This setting also yields the highest aneurysm IoU of 89.24. The highest ostium IoU is achieved with synthetic pretraining followed by fine-tuning on 100 % real data, reaching 13.13. Notably, increasing the amount of real fine-tuning data beyond 50 % does not further improve mIoU, suggesting diminishing returns for this task.

By contrast, the model trained only on synthetic data performs substantially worse on the real test set, with an mIoU of 36.78, an aneurysm IoU of 17.80, and an ostium IoU of 0.38. This is expected given the domain gap, since SynVA-P1 currently generates simplified single-bifurcation anatomies, whereas the real data contain more complex vascular trees with multiple branches. Overall, the results show that synthetic data alone is not sufficient for generalization, but serves as an effective pretraining source.